Microplane model M7 for plain concrete. I: Formulation — **Source link** ⧉

Ferhun C. Caner, Zdenek P. Bazant

Institutions: Northwestern University

Related papers:

- Crack band theory for fracture of concrete

- Microplane Model M7 for Plain Concrete. II: Calibration and Verification

- Microplane Model M4 for Concrete. I: Formulation with Work-Conjugate Deviatoric Stress

- Microplane Model for Progressive Fracture of Concrete and Rock

- Lattice Discrete Particle Model (LDPM) for failure behavior of concrete. I: Theory

Microplane Model M7 for Plain Concrete. I: Formulation

Ferhun C. Caner[1] and Zdeněk P. Bažant, Hon.M.ASCE[2]

Abstract: Mathematical modeling of the nonlinear triaxial behavior and damage of such a complex material as concrete has been a long-standing challenge in which progress has been made only in gradual increments. The goal of this study is a realistic and robust material model for explicit finite-element programs for concrete structures that computes the stress tensor from the given strain tensor and some history variables. The microplane models, which use a constitutive equation in a vectorial rather than tensorial form and are semimultiscale by virtue of capturing interactions among phenomena of different orientation, can serve this goal effectively. This paper presents a new concrete microplane model, M7, which achieves this goal much better than the previous versions M1–M6 developed at Northwestern University since 1985. The basic mathematical structure of M7 is logically correlated to thermodynamic potentials for the elastic regime, the tensile and compressive damage regimes, and the frictional slip regime. Given that the volumetric-deviatoric (V-D) split of strains is inevitable for distinguishing between compression failures at low and high confinement, the key idea is to apply the V-D split only to the microplane compressive stress-strain boundaries (or strain-dependent yield limits), the sum of which is compared with the total normal stress from the microplane constitutive relation. This avoids the use of the V-D split of the elastic strains and of the tensile stress-strain boundary, which caused various troubles in M3–M6 such as excessive lateral strains and stress locking in far postpeak uniaxial extension, poor representation of unloading and loading cycles, and inability to represent high dilatancy under postpeak compression in lower-strength concretes. Moreover, the differences between high hydrostatic compression and compressive uniaxial strain are accurately captured by considering the compressive volumetric boundary as dependent on the principal strain difference. The model is verified extensively in the companion paper. **DOI: [10.1061/(ASCE)EM.1943-7889.0000570](.)**. © *2013 American Society of Civil Engineers.*

CE Database subject headings: Constitutive models; Inelasticity; Cracking; Damage; Concrete; Algorithms; Mathematical models.

Author keywords: Constitutive modeling; Inelastic behavior; Cracking damage; Yield limits; Softening; Concrete; Numerical algorithm; Thermodynamic potentials; Unloading.

Introduction

In 1938, the great G. I. Taylor proposed a new type of hardening plasticity model in which the constitutive law is expressed in terms of not tensors but vectors of stress and strain, acting on a generic plane of arbitrary orientation in the material. Based on this idea, Batdorf and Budianski (1949) developed the so-called slip theory of plasticity with the following key features:

1. The stress vectors on plastic slip planes are statically constrained to the continuum stress tensor, i.e., they are obtained as the tensor projections onto the slip plane.
2. The plastic strain vectors obtained, on all the slip planes, from the stress vectors according to the plastic constitutive law are superposed to yield the continuum plastic strain tensor; and
3. The plastic strain tensor thus obtained is added to the elastic strain tensor calculated according to the elasticity constants from the stress tensor.

This approach has by now led to the most powerful constitutive models for hardening plasticity of polycrystalline metals, broadly called the Taylor models (Butler and McDowell 1998; Rice 1971; Hill and Rice 1972; Asaro and Rice 1977; Brocca and Bažant 2000).

When generalizations to inelastic phenomena other than plastic slip (e.g., the cracking damage) were attempted, the term slip plane became inappropriate, and the more general term microplane was coined (Bažant 1984) to denote a generic plane of any orientation within the material on which the constitutive model is formulated as a relation between the stress and strain vectors. The reason for the prefix micro- is that, unlike the inelastic strain tensor on the continuum level (called the macrolevel), the normal and shear components of an inelastic strain vector on a microplane allow for an intuitive representation of microstructural phenomena such as microcracking and microslipping with friction. In tensorial models, a relation between J_2 and I_1 is regarded as internal friction, but in reality, the frictional slip occurs on specific planes, which only vectorial modeling can capture.

A dual alternative to the static constraint assumed in the Taylor models is the kinematic constraint, which means that the strain vector on a microplane is assumed to be a projection of the strain tensor. The static and kinematic constraints cannot hold simultaneously—only one or the other.

As it turned out, around 1980, the Taylor model with a static constraint was found to be unstable in the presence of softening damage, such as the distributed cracking in concrete. The instability is caused by the localization of softening inelastic strain into a single microplane and additive (or series) coupling of elastic strains on the tensorial level. The problem was remedied in 1983 (Bažant and Oh 1983, 1985; Bažant 1984) by the following three modifications,

[1]Associate Professor, Institute of Energy Technologies, School of Industrial Engineering, Univ. Politecnica de Catalunya, Campus Sud, 08028 Barcelona, Spain; presently, Visiting Scholar, Dept. of Civil and Environmental Engineering, Northwestern Univ., Evanston, IL 60208. E-mail: ferhun.caner@upc.edu

[2]Distinguished McCormick Institute Professor and W. P. Murphy Professor of Civil Engineering, Mechanical Engineering, and Materials Science, Northwestern Univ., Evanston, IL 60208 (corresponding author). E-mail: z-bazant@northwestern.edu

which represent the salient characteristics of the microplane constitutive models for materials with damage:

1. The static constraint must be replaced with a kinematic constraint;
2. Instead of superposition, the continuum stress tensor must be calculated from the stress vectors on all the microplanes by means of the principle of virtual work; and
3. The elastic strains cannot be superposed on the macrolevel (i.e., continuum tensorial level) but must be part of the constitutive law on the microplanes.

The principle of virtual work gives the stress tensor components as integrals over a unit hemisphere whose normals represent all possible microplane orientations. This integral is in computations approximated according to some of the optimal Gaussian integration formulas for a spherical surface, which replaces the integral by a weighted sum over a finite number of microplanes. Accuracy demands the number of microplanes to be at least 21, although preferably at least 37 of them should be used to reduce numerical errors in far postpeak (Bažant and Oh 1986). Because the microplanes sample all possible orientations without bias, the principle of frame indifference is satisfied—for a finite number of microplanes only approximately but in the limit case of an integral exactly.

The microplane models can be regarded as semimultiscale models (Bažant 2010), because they capture the orientation interactions of microscale inelastic deformations. They do not capture the distance interactions, which is attributable to lumping the inelastic phenomena into a single continuum point. Consequently, the microplane models fulfill only half the goal of the now-fashionable multiscale models. However, in the case of strain-softening damage, the existing multiscale models cannot capture the distance interactions either. The reason is that they miss the effects of the localization instabilities on the microscale caused by microcrack interactions and fail to predict the size of the fracture process zone (or the characteristic length, serving as a localization limiter).

The development of microplane models was initially hampered by their greater demand for computer power compared with the classical tensorial models. However, this disadvantage has since evaporated. The computers that exist today can handle systems of tens of millions of finite elements using the microplane model.

Since 1983, a series of progressively improved microplane models labeled M0, M1, M2, . . ., M6 have been developed for concrete, and other microplane models have been developed for clays, soils, rocks, rigid foams, and fiber composites (prepreg laminates and braided) (Bažant et al. 2000; Cusatis et al. 2008; Caner et al. 2011). Model M0 used loading surfaces in terms of both the normal and shear components on a microplane, analogous to the theory of plasticity, but that was soon found to be an unnecessary complication. Model M1 (Bažant and Oh 1983, 1985) was limited to tensile cracking damage. Models M2–M6 were able to model inelastic behavior in compression and, crucially, could distinguish between the case of no confinement or weak enough confinement, which leads to strain softening in compression, and the case of strong enough confinement, which does not. This was achieved in M2 (Bažant and Prat 1988a, b) by splitting the microplane normal strain into its volumetric and deviatoric parts and by imposing on each part [see Bažant et al. (1996) for M3 and Bažant et al. (2000) and Caner and Bažant (2000) for M4] separate strain-dependent strength limits, called the stress-strain boundaries.

The volumetric-deviatoric split, however, brought about other problems—especially, excessive lateral expansion and stress locking in far postpeak uniaxial tension and unrealistic unloading and reloading. The expansion and locking problems were mitigated in M5 (Bažant and Caner 2005a, b) by a series coupling of separate microplane models for compression and for tension. In M6 (Caner and Bažant 2011), this was achieved by a continuous transition to no split at increasing extension but at the price of compromising the large-scale numerical computations, the unloading and loading cycles, and the simultaneous tensile and compression softening in different directions.

Also, in view of the split of microplane strains, it was thought to be desirable (in M4, though not M6) to enforce the macro–micro equilibrium separately for the volumetric and deviatoric stress components. However, this unnecessary hypothesis caused the deviatoric microplane stresses at all the microplanes of M4 not to have a zero volumetric resultant on the macroscale, which had to be corrected by an iterative loop. Abandoning the volumetric-deviatoric split altogether was attempted in microplane model M2' by Hasegawa and Bažant (1993a, b), but the modeling capability proved to be inferior to that of M3 and M4.

All these problems are overcome in the present model M7. The key idea is to abandon the volumetric-deviatoric split for the elastic part of microplane strains and for the tensile stress-strain boundary while retaining it for the compressive normal and deviatoric stress-strain boundaries, which are then summed for comparison with the total normal stress. It will be shown that this idea endows the concrete microplane model with a much better and broader modeling capability than the previous microplane models.

Numerous advantages of microplane models were reviewed in Brocca and Bažant (2000) and Bažant et al. (2000). One advantageous feature that has generally been overlooked in constitutive modeling but that should be emphasized is that the microplane model automatically captures the vertex effect, i.e., the fact that deformation increments that are parallel to the current loading surface in the stress space are not elastic but inelastic, as experimentally demonstrated in Caner et al. (2002). This effect comes into play when the principal stress and strain directions rotate against the material, which is a typical occurrence, especially under dynamic loads. Tensorial models with one or a few loading surfaces cannot capture this effect as a matter of principle. Why can the microplane model?—Because it effectively represents multisurface plasticity with several vectorial limit surfaces at each microplane.

Another important advantage is that, in the vectorial component form on a generic microplane, it is easy to take into account the strain dependence of the yield limit. In tensorial form, it would be preposterously complex to do that.

It must also be stressed that the microplane model provides only the constitutive (or stress-strain) relation. Because of postpeak softening, in practical applications, it must be combined with some localization limiter, such as the nonlocal or crack band models. In this way, M7 provides the stress-separation relation for a cohesive crack, enhanced by the effect of shear and longitudinal compression along the crack, and also gives a realistic transitional size effect (Bažant and Yu 2011).

Finally, it is worth noting that the constitutive relations prescribed on the microplanes, which are lumped into a single material point in the microplane models, can also be used in an explicitly mesoscale model on planes of various orientations separating the neighboring aggregates embedded in a cement mortar matrix. This is done in the lattice discrete particle model (LDPM), which evolved from the initial attempt in Cusatis et al. (2003). Inevitably, there are similarities between the constitutive relations of microplane models and those of LDPM. In the latest, simultaneously and independently developed version of the LDPM (Cusatis et al. 2011b, a), the compressive normal boundary is constructed without using any separate deviatoric and volumetric boundaries, and the boundary on the normal strains is defined as a function of both the volumetric and deviatoric strains. In this sense, there is a partial analogy with one basic idea of model M7, which is not to calculate any separate

volumetric and deviatoric stress components and use the sum of the compressive volumetric and deviatoric boundaries as a boundary imposed on the total compressive normal stress on the microplanes.

Basic Relations for Kinematically Constrained Microplanes

Unlike the classical tensorial constitutive models, the microplane constitutive model is defined by a relation between the stresses and strains acting on a generic plane of any orientation in the material, called the microplane. The basic hypothesis, which was shown in Bažant (1984) to be necessary to ensure the stability of the postpeak strain softening (and which leads to a robust explicit algorithm), is that the strain vector $\boldsymbol{\varepsilon}_N$ on the microplane [Fig. 1(a)] is the projection of $\boldsymbol{\varepsilon}$, i.e., $\varepsilon_{N_i} = \varepsilon_{ij} n_j$, where n_i are the components of the unit normal vector $\mathbf{n}$ of the microplane, with the subscript i referring to the global Cartesian coordinates x_i ($i = 1, 2,$ and 3). The authors also introduce orthogonal unit coordinate vectors $\mathbf{m}$ and $\mathbf{l}$, of components l_i and m_i, lying within the microplane [Fig. 1(a)]. Taking the projections of vector $\boldsymbol{\varepsilon}_N$ onto n_i, l_i, and m_i, one gets the normal and shear strain components and the shear strain resultant

$$\varepsilon_N = N_{ij}\varepsilon_{ij}, \quad \varepsilon_L = L_{ij}\varepsilon_{ij}, \quad \varepsilon_M = M_{ij}\varepsilon_{ij} \qquad (1)$$

$$\varepsilon_T = \sqrt{\varepsilon_L^2 + \varepsilon_M^2} \qquad (2)$$

where

$$N_{ij} = n_i n_j, \quad L_{ij} = (l_i n_j + l_j n_i)/2, \quad M_{ij} = (m_i n_j + m_j n_i)/2 \qquad (3)$$

The subscript N refers to the normal direction n_i; subscripts L and M refer to the shear directions l_i and m_i; and subscript τ refers to the shear resultant. Repetition of subscripts implies summation over $i = 1, 2,$ and 3. A vector $\mathbf{m}_i$ may, for example, be chosen to be normal to the x_3-axis, in which case $m_1 = n_2(n_1^2 + n_2^2)^{-1/2}$, m_2

$= -n_1(n_1^2 + n_2^2)^{-1/2}$, $m_3 = 0$, but $m_1 = 1$ and $m_2 = m_3 = 0$ if $n_1 = n_2 = 0$. A vector $\mathbf{m}_1$ normal to $\mathbf{x}_1$ or $\mathbf{x}_2$ may be obtained by permutations of the indexes 1, 2, and 3. The orthogonal unit vector is generated as $\mathbf{l} = \mathbf{m} \times \mathbf{n}$. To minimize directional bias, vectors $\mathbf{m}$ are alternatively chosen to be normal to the x_1-, x_2-, or x_3-axes. To model softening damage in compression (though not in tension), it is helpful to define the deviatoric normal strains ε_D on the microplanes

$$\varepsilon_D = \varepsilon_N - \varepsilon_V, \quad \varepsilon_V = \varepsilon_{kk}/3 \qquad (4)$$

where ε_V = volumetric strain (or mean strain), which is the same for all the microplanes (whereas ε_D is not).

In general, it is impossible for both the stress and strain vectors on the microplanes to be the projections of the stress and strain tensors. Therefore, the static equivalence, or equilibrium, between the stress vectors on all the microplanes and the stress tensor must be enforced variationally based on the principle of virtual work (Bažant 1984), which may be written as

$$\frac{2\pi}{3}\sigma_{ij}\delta\varepsilon_{ij} = \int_\Omega (\sigma_N\delta\varepsilon_N + \sigma_L\delta\varepsilon_L + \sigma_M\delta\varepsilon_M)\mathrm{d}\Omega \qquad (5)$$

where Ω = surface of a unit hemisphere centered at the material point; and $2\pi/3$ = its volume. This equation means that the virtual work of continuum stresses (or macrostresses) within a unit sphere must be equal to the virtual work of the microplane stress components (or microstresses) regarded as the tractions on the surface of the unit sphere. The integral may be regarded as orientational homogenization of the contributions from planes of various orientations within the material, as depicted in Fig. 1(b) [for a detailed physical justification, see Bažant et al. (1996)]. Substituting $\delta\varepsilon_N = N_{ij}\delta\varepsilon_{ij}$, $\delta\varepsilon_L = L_{ij}\delta\varepsilon_{ij}$, and $\delta\varepsilon_M = M_{ij}\delta\varepsilon_{ij}$ and noting that the last variational equation must hold for any variation $\delta\varepsilon_{ij}$, one gets the following basic equilibrium relation (Bažant 1984):
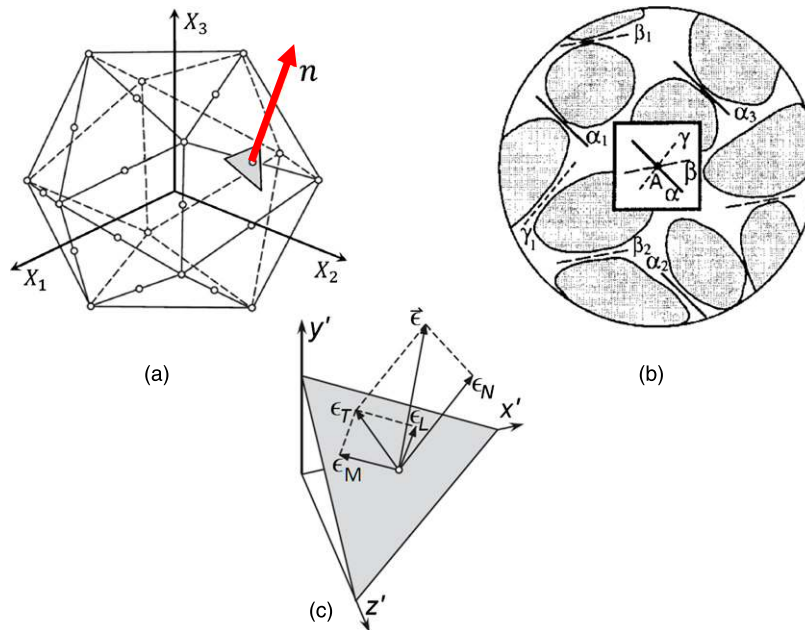

Fig. 1. (a) Microplane strain vector and its components; (b) system of discrete microplanes; (c) microplane strain components

$$\sigma_{ij} = \frac{3}{2\pi} \int_{\Omega} s_{ij} d\Omega \approx 6 \sum_{\mu=1}^{N_m} w_\mu s_{ij}^{(\mu)} \qquad (6)$$

$$s_{ij} = \sigma_N N_{ij} + \sigma_L L_{ij} + \sigma_M M_{ij} \qquad (7)$$

In numerical calculations, this integral is approximated by an optimal Gaussian integration formula for a spherical surface (Stroud 1971; Bažant and Oh 1985) representing a weighted sum over the microplanes of orientations $\mathbf{n}_\mu$, with weights w_μ normalized so that $\sum_\mu w_\mu = 1/2$ (Bažant and Oh 1985, 1986). The most efficient formula that still yields acceptable accuracy involves 21 microplanes [Bažant and Oh 1986; Fig. 1(b)], although to get better accuracy in far postpeak softening, 37 microplanes are currently preferred. In finite-element programs, the integral given in Eq. (6) approximated by a sum must be evaluated at each integration point of each finite element in each time step. The values of $N_{ij}^{(\mu)}$, $M_{ij}^{(\mu)}$, and $L_{ij}^{(\mu)}$ for all the microplanes $\mu = 1, \ldots, N_m$ are common to all the integration points of all finite elements and are calculated and stored in advance.

The most general explicit constitutive relation on the microplane level may be written as

$$\sigma_N(t) = \mathcal{F}_{\tau=0}^t[\varepsilon_N(\tau), \varepsilon_T(\tau)], \quad \sigma_L(t) = \mathcal{G}_{\tau=0}^t[\varepsilon_N(\tau), \varepsilon_T(\tau)],$$
$$\sigma_M(t) = \mathcal{H}_{\tau=0}^t[\varepsilon_N(\tau), \varepsilon_T(\tau)] \qquad (8)$$

where $\mathcal{F}$, $\mathcal{G}$, and $\mathcal{H}$ = functionals of the history of the microplane strains at time t; and $\varepsilon_T(\tau)$ = shear strain resultant with components ε_M and ε_L. The functionals $\mathcal{G}$ and $\mathcal{H}$ are the same except that they give different projections on axes L and M.

Elastic Behavior and Material Damage for Unloading

When the normal microplane strains ε_{N_μ} are not split into their volumetric and deviatoric parts, ε_V and ε_{D_μ}, with independent elastic constants for each, the normal and shear stiffness constants E_N and E_T on the microplanes under a kinematic constraint are [Bazant and Prat 1988a, Eq. (22); Carol and Bažant 1997, Eq. (32)]

$$E_N = \frac{E}{1-2\nu}, \quad E_T = E_N \frac{1-4\nu}{1+\nu} \qquad (9)$$

where E = Young's modulus on the macrolevel; ν = Poisson's ratio; and $E_N = K/3$ where K is the bulk modulus. Because both E_N and E_T must be nonnegative, only Poisson's ratios in the range $\nu \in [-1, 0.25]$ can be reproduced.

This range of ν is sufficient for concrete, for which $\nu \approx 0.18$, but would not suffice for some other materials with $\nu \in (0.25, 0.5]$, such as metals, ceramics, polymers, or ice. For those, one easy remedy, mentioned in Bažant and Oh (1985), is to make the microplane model coupled in parallel with an isotropic volumetric elastic element that is subjected to the same strain tensor ε_{ij} and has a finite bulk modulus K' but zero shear modulus $G' = 0$ (Fig. 2). Because, for such a coupled model, the bulk and shear moduli are $\tilde{K} = K + K'$ and $\tilde{G} = G + G' = G$, Poisson's ratio is (Fung 1968, p. 130)

$$\tilde{\nu} = \frac{3K(1 + G/G') - 2G}{6K(1 + G/G') + 2G} \qquad (10)$$

which tends to 0.5 when $G'/G \to 0$. Any Poisson's ratio up to 0.5 can thus be reproduced (without a volumetric-deviatoric split).
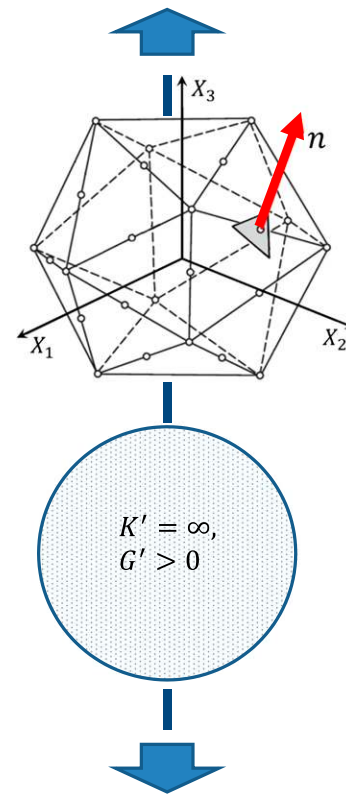
Fig. 2. Microplane system coupled to an element with infinite volumetric stiffness, making possible any thermodynamically admissible value of Poisson ratio (in the present model for concrete, $G' = \infty$, i.e., the coupled element is rigid, and the strain in the microplane model is the total strain)

In the present modeling of concrete, the coupling of such a parallel element is not necessary, and so, it is not made here. Nevertheless, $\nu = 0.18$ could also be obtained with such coupling when E_N and E_T are tuned to give less than 0.18 without the coupling. It seems that the present modeling capability would not be enhanced by such coupling, but this is one point that may be worth checking further (especially for a material with ν less than, but close to, 0.25).

In microplane models M1 and M2, the tangential microplane stiffness was varied as a function of strain. However, beginning with model M3 (Bažant et al. 1996), it appeared simpler to introduce strain-dependent strength (or yield) limits, called stress-strain boundaries. Within the boundaries, the response is elastic, with constant microplane elastic stiffness E_N and E_T.

The fact that the stress-strain boundary is reached at different microplanes at different moments of loading is what causes both the prepeak and postpeak macrolevel stress-strain curves to vary their slope gradually, as observed in experiments. Similarly, during macroscopic unloading, different microplanes return from the stress-strain boundary into the elastic domain at different moments, which again causes the unloading curves to change unloading slope gradually, with a progressively decreasing slope as the unloading proceeds. Similar comments apply to reloading.

Energy Dissipation

Thermodynamically sound constitutive models must obviously satisfy the condition that the density of the dissipation rate must be nonnegative. In microplane models, this criterion could easily be

satisfied by requiring the dissipation rate on each microplane to be nonnegative. However, there are three problems with this requirement.

1. The dissipation rate on each microplane being nonnegative is only a sufficient condition, not a necessary one; only the combined dissipation rate on the microplane system must be nonnegative, which means that the dissipation can be negative on some microplanes.
2. Purely elastic unloading on the macrolevel is not realistic, and so, the effect of damage attributable to material stiffness loss must be known. Depending on the future unloading path, one can judge the current energy dissipation rate to be positive or negative.
3. On the macrolevel, the unloading path is complex and curved, because different microplanes start unloading at different times rather than simultaneously.

Is it important to distinguish between sufficient and necessary? It is. Previously, in Bažant et al. (2010), an automatic correction in each loading step of a microplane model was developed to satisfy the dissipation criterion on each microplane separately, which is a sufficient, though not necessary, way to satisfy the dissipation inequality. But such a correction was subsequently found to be far too stringent, making it impossible to fit most test data.

The density of the energy dissipation increment may be written as $d\mathcal{D} = dW - dU$ where $dW = \sigma_{ij}d\varepsilon_{ij}$ is the work of stress on the strain increments and U is the density of recoverable stored energy. Unfortunately, the value of U cannot be defined at the current state, because in a general microplane model, it depends on the stress-strain histories for loading and future unloading, the latter being unknown in advance.

To illustrate the difficulty, consider [similar to Bažant et al. (2010)] one tensorial component of the stress and strain only and a general stress-strain diagram with strain softening, $\sigma(\varepsilon)$, as shown in Fig. 3. An infinitesimal strain increment $d\varepsilon$ from point 1 to point 2 leads to material damage that causes (in the presence of continuing damage) the unloading path to change from curve $\overline{14}$ to curve $\overline{23}$. Curve $\overline{64}$ is a rigid-body shift of $\overline{23}$ to the left. Because $d\varepsilon$ is infinitesimal, $\overline{51}$ is also infinitesimal. So, the work given by the triangle $\overline{1251}$ is second-order small, infinitely smaller than the cross-hatched areas, and thus negligible. Area $\overline{23462}$ is the inelastic work increment $dW = \sigma d\varepsilon''$ representing the inelastic (or plastic) part of energy dissipation. Area $\overline{4564}$ is the decrement of stored energy, $dU (< 0)$, which represents the energy dissipation attributable to damage. The total energy dissipation increment is $d\mathcal{D} = dW + (-dU)$ and is represented by the combined cross-hatched area $\overline{456234}$. So, in this one-component setting (Fig. 3), a sufficient requirement of nonnegative energy dissipation would be that the combined (cross-hatched) area $\overline{23452}$ be nonnegative.
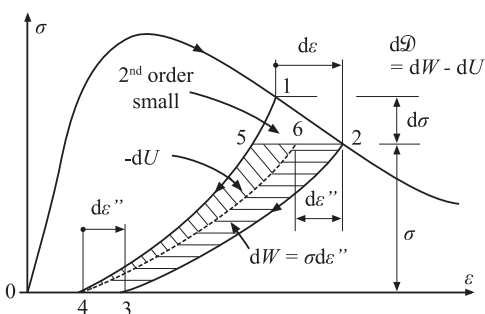
But for the microplane system as a whole, this condition cannot be evaluated in the current state, because the shape of the future unloading paths $\overline{154}$ and $\overline{26}$ is not known, as different microplanes transit to unloading at different times, giving a curved unloading path (which is the actual behavior of concrete). This contrasts with the classical plastic or damage theories in which the unloading behavior is known and simple—either a straight line of elastic unloading or a straight line through the origin or a combination of the two.

This is one difficulty. Another is that a realistic check for nonnegative dissipation must include multiaxial stress paths, such as a closed loop consisting of normal stress increment, shear stress increment, normal stress decrement, and shear stress decrement returning to the original zero stress tensor.

An example of such a loop was given in Carol et al. (2001) for microplane model M2, with the conclusion that energy dissipation could be negative. However, the unloading path was considered in that example to be a straight line always pointed to the origin, which is unrealistic and is not the way model M2 has been used. If the unloading in that example is assumed to follow a constant elastic stiffness, no problem occurs for M2.
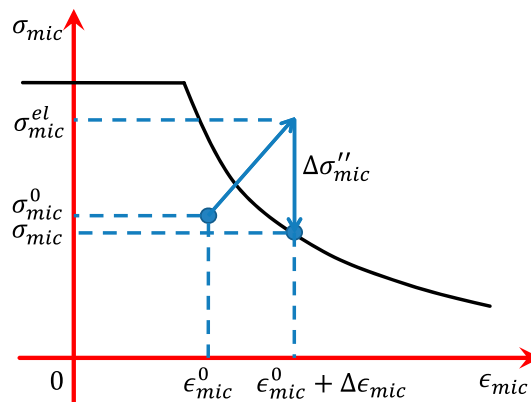
For the present model M7, computations have been run for some similar closed loops, and no negative dissipation has been found, but a general dissipation check for M7, covering all the possible loops, is a challenge.

Microplane Stress-Strain Boundaries and Numerical Algorithm

Damage corresponding to the orientation of a given microplane is characterized by compressive volumetric and deviatoric boundaries σ_V^b and σ_D^b and by the tensile normal boundary σ_N^b. If the boundary is exceeded in a finite load or time step, the stress is reduced to the boundary keeping the strain constant, as illustrated for σ_N in Fig. 4.

Rather than explaining the boundaries first, it will be more effective to do so after presenting the computational algorithm. The algorithm for each load or time step uses the values of increments $\Delta\varepsilon_{ij}$ for the current step and the values of ε_{ij}^o and σ_{ij}^o for the end of the previous step. The subscript 0 is attached in E_0 and E_{N0} to denote the original (initial, undamaged) values of E and E_N, whereas the superscript o labels, when necessary, the values at the beginning of the current step (which is also the end of the previous step).

At each integration point of each element in each load or time step of an explicit finite-element program, there is a loop over all the

Fig. 3. Dependence of energy dissipation in strain-softening materials on the unloading behavior

Fig. 4. Vertical return to stress-strain boundary at constant strain when the boundary is exceeded by elastic stresses in a finite load step

microplanes in which the new stress tensor σ_{ij} at the end of the current step is computed as follows:

1. First, evaluate the microplane strains from Eq. (2) and the microplane strain increments as

$$\Delta\varepsilon_N = N_{ij}\Delta\varepsilon_{ij}, \quad \Delta\varepsilon_M = M_{ij}\Delta\varepsilon_{ij}, \quad \Delta\varepsilon_L = L_{ij}\Delta\varepsilon_{ij} \quad (11)$$

2. Calculate the volumetric strain at the end of the previous step, its increment, and the volumetric strain at the end of current step

$$\varepsilon_V^o = \varepsilon_{kk}/3, \quad \Delta\varepsilon_V = \Delta\varepsilon_{kk}/3, \quad \varepsilon_V = \varepsilon_V^o + \Delta\varepsilon_V \quad (12)$$

3. Evaluate $\varepsilon_e = \langle -\sigma_V^o/E_{N0}\rangle$ [where $\langle x\rangle = \max(x, 0) = $ Macauley brackets], and get the corresponding value of the volumetric stress-strain boundary

$$\sigma_V^b = -Ek_1 k_3 e^{-\varepsilon_V/k_1\alpha} \quad (13)$$

where

$$\alpha = \frac{k_5}{1 + \varepsilon_e}\left(\frac{\varepsilon_I^o - \varepsilon_{III}^o}{k_1}\right)^{c_{20}} + k_4 \quad (14)$$

in which k_i ($i = 1, 2,$ and 3) $=$ adjustable scaling parameters whose numerical values will be discussed later, and ε_I^o and ε_{III}^o $=$ maximum and minimum principal strains at the beginning of the step.

4. Calculate the deviatoric strain components on the microplane

$$\Delta\varepsilon_D = \Delta\varepsilon_N - \Delta\varepsilon_V, \quad \varepsilon_D^o = \varepsilon_N - \varepsilon_V^o, \quad \varepsilon_D = \varepsilon_D^o + \Delta\varepsilon_D \quad (15)$$

and the value of the compressive deviatoric stress-strain boundary (which is negative)

$$\sigma_D^b = -\frac{Ek_1\beta_3}{1 + \left[\langle -\varepsilon_D\rangle/(k_1\beta_2)\right]^2} \quad (16)$$

where

$$\beta_2 = c_5\gamma_1 + c_7, \quad \beta_3 = c_6\gamma_1 + c_8, \quad \gamma_0 = f_{c0}'/E_0 - f_c'/E \quad (17)$$

$$\gamma_1 = e^{\gamma_0}\tanh(c_9\langle -\varepsilon_V\rangle/k_1) \quad (18)$$

5. Calculate the new (end of step) value of $\varepsilon_N = \varepsilon_V + \varepsilon_D$, and retrieve the stored positive and negative normal strains of maximum magnitudes reached so far, ε_N^{0+} and ε_N^{0-} (history variables). Then, denoting $E_{N0} = E/(1 - 2\nu)$, calculate the current damaged value of the normal microplane elastic modulus

$$E_N = E_{N0}e^{-c_{13}\varepsilon_N^{0+}}f(\zeta) \quad \text{for } \sigma_N^o \geq 0 \quad (19)$$

but

$$E_N = E_{N0} \quad \text{if } \sigma_N^o > E_{N0}\epsilon_N \text{ and } \sigma_N^o\Delta\epsilon_N < 0 \quad (20)$$

$$E_N = E_{N0}\left(e^{-c_{14}|\varepsilon_N^{0-}|/(1+c_{15}\varepsilon_e)} + c_{16}\varepsilon_e\right) \quad \text{for } \sigma_N^o < 0 \quad (21)$$

In Eq. (19), $f(\zeta) = (1 + a\zeta^2)^{-1}$ in which $\zeta = \int\langle d\epsilon_V\rangle$ and typically $a = 0.1$ has been employed to extend the validity of

the model to many load cycles, with virtually no effect for the first few cycles (K. Kirane and Z. P. Bažant, personal communication, 2013). When unloading occurs on the microplanes with normals in the direction of the maximum principal tensile strain, the response inevitably will intersect the initial elastic loading path. This is because of the damage to (or reduction of) the elastic stiffness. The condition in Eq. (20) makes sure that, after the intersection, the unloading proceeds with the initial elastic slope toward the origin, instead of continuing to follow the original unloading path even after the intersection. Following the original unloading path after the two paths intersect would be incorrect, because it would cause negative dissipation during load cycles.

Now, calculate the elastic normal microplane stress

$$\sigma_N^e = \sigma_N^o + E_N\Delta\varepsilon_N \quad (22)$$

6. For $\sigma_N^b > 0$ and with the notation $E_{N0} = E/(1 - 2\nu)$, calculate the value of the tensile normal boundary

$$\sigma_N^b = Ek_1\beta_1 e^{-\langle\varepsilon_N - \beta_1 c_2 k_1\rangle/[-c_4\varepsilon_e\text{sgn}(\varepsilon_e)+k_1 c_3]}$$
$$\text{where } \beta_1 = -c_1 + c_{17}e^{-c_{19}\langle\varepsilon_e - c_{18}\rangle} \quad (23)$$

7. Enforce the vertical drop of stress at constant strain to the stress-strain boundary for normal stress

$$\sigma_N = \max\left[\min\left(\sigma_N^e, \sigma_N^b\right), \sigma_V^b + \sigma_D^b\right] \quad (24)$$

8. If the normal stress-strain boundary has been exceeded, store the overall maxima of normal microplane strain as ε_N^{0+} and ε_N^{0-}.

9. Calculate the approximate average value of all the normal microplane stresses as the current volumetric stress

$$\sigma_V \approx \frac{1}{2\pi}\sum_{\mu=1}^{N_m} w_\mu\sigma_N \quad (25)$$

10. Retrieve the stored previous microplane shear stresses in the L- and M-directions, σ_L^o and σ_M^o. Then, evaluate E_T from Eq. (9) and

$$\hat{\sigma}_N^o = \langle E_T k_1 c_{11} - c_{12}\langle\varepsilon_V\rangle\rangle \quad (26)$$

Now, calculate the shear boundary

$$\sigma_\tau^b = \left[\left(c_{10}\langle\hat{\sigma}_N^o - \sigma_N\rangle\right)^{-1} + \left(E_T k_1 k_2\right)^{-1}\right]^{-1} \quad \text{for } \sigma_N \leq 0 \quad (27)$$

$$\sigma_\tau^b = \left[\left(c_{10}\hat{\sigma}_N^o\right)^{-1} + \left(E_T k_1 k_2\right)^{-1}\right]^{-1} \quad \text{for } \sigma_N > 0 \quad (28)$$

11. Then, calculate the shear response with return to the boundary

$$\sigma_\tau^e = \sqrt{\left(\sigma_L^o + E_T\Delta\varepsilon_L\right)^2 + \left(\sigma_M^o + E_T\Delta\varepsilon_M\right)^2} \quad (29)$$

$$\sigma_\tau = \min\left(\sigma_\tau^b, |\sigma_\tau^e|\right) \quad (30)$$

$$\sigma_L = \left(\sigma_L^o + E_T\Delta\varepsilon_L\right)\sigma_\tau/\sigma_\tau^e \quad (31)$$

$$\sigma_M = \left(\sigma_M^o + E_T\Delta\varepsilon_M\right)\sigma_\tau/\sigma_\tau^e \quad (32)$$

12. Now, calculate the stress tensor σ_{ij} using the sum over all the microplanes in Eq. (6) with Eq. (7), and finally, update the variables σ_V, σ_N, σ_L, σ_M, ε_N^{0+}, and ε_N^{0-}.

The parameters k_i and c_j are empirical and are of two kinds: $k_1, \ldots, k_5$ are free and easily adjustable, and $c_1, \ldots, c_{20}$ are fixed and hard to adjust. Both kinds are discussed in the companion paper.

As a result of delaying the value of σ_V by one step, the foregoing algorithm can exhibit, in regard to the influence of σ_V, only first-order convergence on refining the loading step. A second-order convergence could be achieved by iterating each loading step once (similar to the Runge-Kutta algorithm) and using for σ_V the average value obtained in the first iteration of the step.

Discussion of Stress-Strain Boundaries, Algorithm, and Scaling

In the present model M7, the tensile deviatoric boundary used in M3–M6 is no longer needed. Model M7 employs only four types of stress-strain boundaries:

1. Normal, imposed only on tensile strains [Eq. (23), Fig. 5(a)];
2. Volumetric, imposed only on compressive strains [Eq. (13), Fig. 5(b)];
3. Deviatoric, imposed only on compressive strains [Eq. (16), Fig. 5(c)]; and
4. Plastic-frictional, imposed on the resultant magnitude of the shear stresses and dependent on ε_N (which represents friction) as well as ε_V [Fig. 5(d)].

When σ_N exceeds the boundary, it is dropped to the boundary at constant ε_N. When the resultant σ_T exceeds the boundary, it is dropped to the boundary while keeping both ε_N and ε_V constant (which is a vertical drop in Fig. 4). The new boundary value of shear stress σ_τ^b is then transferred into components σ_L and σ_M in the proportion of the original shear stress vector components augmented by elastic shear stress increments in the step [Eqs. (31) and (32)].

In contrast to the present model, in previous microplane models M4–M6 the shear boundary was applied separately to each component σ_L and σ_M, and the dependence of the components σ_L and σ_M on the

choice of coordinates was countered in the overall sense by selecting the coordinates randomly on each microplane. This approach was motivated empirically by the fact that it led to a more realistic, large enough ratio of biaxial to uniaxial compressive strength. However, it now appears that imposing the boundaries on the components was needed because of adverse effects of the elastic volumetric-deviatoric split. In the present model without such a split, the biaxial strength is simulated correctly despite imposing the boundary on the shear resultant. Thanks to applying the boundary on the shear resultant, the directional dependence of the response is removed completely, even at the microplane level. (Previously, it was removed only statistically in the mean, by alternating the in-plane coordinate directions over all the microplanes.)

The crucial innovation compared with models M3–M6 that greatly enhances the modeling power is that in compression the volumetric and deviatoric boundaries, rather than being used to limit σ_V^b and σ_D^b separately, are used [in Eq. (24)] only to limit σ_N by the sum $\sigma_N^b = \sigma_V^b + \sigma_D^b$. By contrast with the preceding models M3–M6 in which the volumetric-deviatoric split of microplane normal stress was introduced in the elastic behavior and generally did not hold in the inelastic range, in the current model this split applies only in the inelastic range. This innovation makes it possible to dispense with the volumetric-deviatoric split of the elastic deformations, which led in M3–M6 to problems with the tensile response, such as excessive lateral expansions and normal stress locking at far postpeak extensions.

Although this innovation first transpired heuristically, it logically follows from the hypothesis that the elastic and damage potentials, U and Ψ, have the form introduced in Eqs. (33) and (35), in which Ψ depends on both ε_N and ε_V separately while U depends only on ε_N. Indeed, Eq. (42) implies that the sum $\sigma_V^b + \sigma_D^b$ ought to appear in Eq. (23) for the normal boundary.

Introducing the volumetric-deviatoric split only for the damage-controlling normal boundary, and not for the elastic behavior, has made it possible to get rid of the tensile deviatoric boundary, which had to be used in M4–M6 to avoid two related problems in far postpeak extension under uniaxial stress: (1) excessive lateral expansion, and (2) axial stress locking, which means that the axial stress does not reach zero at very large tensile strain and may even begin to rise. Such problems were traced in M4 to the nonuniqueness
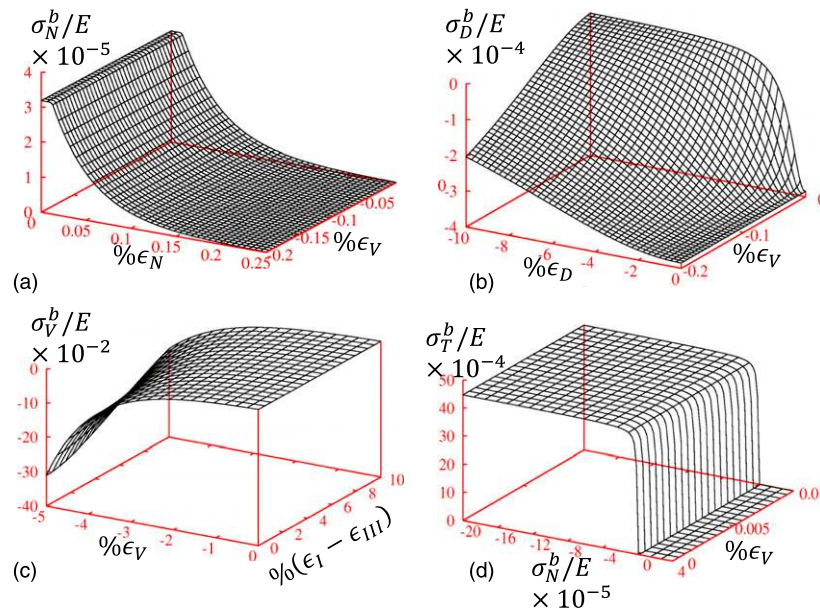
Fig. 5. Stress-strain boundaries used in model M7: (a) normal boundary; (b) deviatoric boundary; (c) volumetric boundary; (d) plastic-frictional boundary

J. Eng. Mech. 2013.139:1714-1723.

of the subdivision of elastic normal strain into its elastic volumetric and deviatoric parts. In M4, it could happen that the postpeak normal stress would be reduced to zero while both the volumetric and deviatoric parts were large, of opposite signs, and cancelling each other. It was this feature that caused both the excessive lateral expansion and stress locking.

The volumetric stress σ_V^o as a parameter for the normal boundary in Eq. (23) has been useful for data fitting, particularly to ensure that the postpeak compression under uniaxial stress would not be too steep. The use of σ_V, of course, destroys full explicitness in calculating the normal stress from the strain. Thus, the value of σ_V^o needs to be computed from the microplane stress values obtained at the end of the previous step, or the current step must be iterated to estimate the average σ_V^o for the current load step.

A further feature different from M4 (but introduced already in M6) is the use of the maximum principal strain difference $\varepsilon_I - \varepsilon_{III}$ as a parameter for the volumetric boundary. This difference does no work on the volumetric stress σ_V and thus does not represent a kinematic variable of the volumetric boundary (which is why it is absent from the potentials in the Appendix). From the thermodynamic viewpoint, the fact that the difference $\varepsilon_I - \varepsilon_{III}$ does zero work during volume change makes its role similar to the role of nonworking normal stress or normal strain during nondilatant frictional slip.

The difference $\varepsilon_I - \varepsilon_{III}$ is needed to distinguish weakly confined or unconfined compression, which terminates with strain softening (as under compressive uniaxial or biaxial stress), from highly confined compression, which does not (as in uniaxial strain and hydrostatic compression). Of course, the use of ε_D helps to make the same distinction, as in M4, but ε_D alone is not enough.

Another useful new feature of M7 is that the use of the principal strain difference as a parameter of the volumetric boundary [Eqs. (13) and (14)] helps to distinguish the behaviors of low-strength and normal-strength concretes. Because this difference is zero under hydrostatic (or volumetric) compression and nonzero, with growing magnitude, under confined compression, it also helps to distinguish between the hydrostatic compression and the perfectly confined uniaxial compression (or uniaxial strain). In models M3 and M4, this important distinction could not be made, in general.

The plastic-frictional boundary [Fig. 5(d)] at small compression σ_N has a steep slope, indicating a high frictional effect. At zero σ_N, the boundary allows transmission of nonzero σ_T, representing cohesion. The shear resistance σ_T vanishes at finite tensile stress, the value of which depends on ε_V [Fig. 5(d)]. When $\varepsilon_V \gg 0$, the cohesion vanishes. The effect of ε_V disappears under large enough compressive σ_N. At very large compressive σ_N, the boundary has almost no slope. This means that, under high confinement, concrete becomes perfectly plastic, a fact that has been established by tube-squash tests (Bažant et al. 1999; Caner and Bažant 2002). This feature is, for instance, important for energy dissipation under the nose of a penetrating missile, where extreme pressures may develop.

The β-coefficients in boundary Eqs. (16), (17), and (23) take empirically into account the transition from low-strength concrete to normal-strength concrete. Let f_{c0}' be the chosen reference strength in compression. For $f_c' = f_{c0}'$, one has the deviatoric boundary for the low-strength concrete, for which the volumetric boundary depends strongly on the deviatoric strain, and for $f_c' \gg f_{c0}'$, one has the deviatoric boundary for normal-strength concrete, for which this dependence is mild. This distinction is important for low-strength concretes, because such concretes exhibit a much stronger dilatancy during shearing. As the strength increases, the dilatancy diminishes, and it probably totally disappears for very high strength concretes, which are extremely brittle and fail by smooth cracks and with small fracture process zones.

The current formulation without a volumetric-deviatoric split of elastic strains, as given by Eqs. (19)–(21), leads to realistic unloading and reloading responses for both tension and compression. To explain why it does, consider unloading that starts when the axial tensile strain is in the postpeak softening regime. On the microplane level, only those microplanes whose normals form a sufficiently small angle with the maximum principal strain direction have reached the postpeak regime, and thus, a reduced unloading stiffness is prescribed only for those [Eq. (19)]. The microplanes whose angle with this direction is sufficiently large still remain in the elastic regime, and so, they unload with the high slope of the initial elastic stiffness. Consequently, the unloading slope is not the same for all the microplanes even if the normal stress is positive on all the microplanes, and a certain compromise slope gets manifested on the macroscale. Different microplanes switch from loading to unloading at different times. This causes the start of unloading on the macroscale to be curved, with a positive curvature.

As the macroscale unloading proceeds from tension to compression, the transition from positive to negative microplane stress occurs at different microplanes at different times. This again causes the slope of unloading on the macroscale to increase gradually, causing the macroscale single-point simulation of this transition to be smoothly, and negatively, curved.

In finite-element simulations of test specimens, a random mesh has been used, except when it proved too difficult to mesh the specimen with a random mesh, as in the vertex effect simulations. The randomness causes different elements to exhibit the loading-unloading and tension-compression transitions at different times even if the stress and strain fields are uniform. As a result, the transitions in the load-unload cycles of whole specimens become even more smooth [see Fig. 4 and the fits in the companion paper (Caner and Bažant 2013)].

Closing Comment

The present paper developed the theoretical formulation. The calibration and verification of model M7 for concrete and the formulation of conclusions from both parts of this study are relegated to the companion paper (Caner and Bažant 2013).

Appendix. Potentials for Elastic, Cracking Damage, and Plastic-Frictional Behaviors

The basic form of a simple microplane model can be obtained by assuming that the density of the dissipative potential of the continuum is a sum of corresponding potentials associated with the individual microplanes (Carol et al. 2001; Bažant et al. 2010). However, for a realistic but complex microplane model such as the present one, the dissipative potentials on the microplanes are difficult to formulate and have not been presented in previous studies of the preceding models. Therefore, instead of attempting the standard thermodynamic approach with a single dissipative free-energy potential (Jirásek and Bažant 2002, Chapter 23), it will merely be shown that it is possible to formulate separate potentials on the macrocontinuum level whose derivatives yield the stress-strain boundaries on the microplanes. The existence of such potentials implies certain symmetry properties that are important for numerical analysis. These potentials may be written as follows:

$$U = \sum_{\nu=1}^{N_m} w_\nu U_\nu(\varepsilon_{N\nu}, \varepsilon_{T\nu}) \tag{33}$$

$$\Pi = \sum_{\nu=1}^{N_m} w_\nu \Pi_\nu(\varepsilon_{N\nu}) \tag{34}$$

$$\Psi = \Psi_V(\varepsilon_V) + \sum_{\nu=1}^{N_m} w_\nu \Psi_\nu(\varepsilon_{N\nu}) \tag{35}$$

$$\Phi = \sum_{\nu=1}^{N_m} w_\nu \Phi_\nu(\dot\varepsilon_{T\nu}; \sigma_{N\nu}, \varepsilon_V) = \sum_{\nu=1}^{N_m} w_\nu \sigma_{T\nu}(\sigma_{N\nu}, \varepsilon_V)\dot\varepsilon_{T\nu} \tag{36}$$

where the overdot denotes the rate with respect to the loading parameter or time; U = elastic potential density (or Helmholtz free energy per unit mass); Π = tensile damage potential density; Ψ = compressive damage potential density; Φ = frictional-plastic potential density; Π, Ψ, and Φ = dissipation potentials whose differentiation gives dissipative stresses of two different types; and Ψ and Φ = stress-strain relations for movement along the damage and frictional boundaries. The transition between the elastic regime and the damage or frictional regime is decided by the inequalities appearing within the computational algorithm.

The expression $\sigma_{T_\mu}(\sigma_{N_\mu}, \varepsilon_V)$ means that frictional stress σ_{T_μ} is a function of both the microplane normal stress σ_{N_μ} and the volume change ε_V. Since σ_{N_μ} does no work on slip, it cannot be derived from the slip potential and represents a friction controlling parameter rather than an independent variable (Bažant and Cedolin 1991, Section 10.7). The reason why σ_{N_μ} and ε_V (or σ_V) do no work is that the microplane slip is considered to occur at no normal strain, i.e., with no dilatancy. This simplification is possible because the dilatancy on the macrolevel is obtained automatically by virtue of cracking damage interaction between microplanes of different orientations and a difference between the tensile and compressive microplane strength limits (Bažant and Gambarova 1984, Figs. 1(a–d); Bažant et al. 2000, Figs. 1(a–d)].

Differentiation of the potentials yields, under various regimes, the stresses at a generic microplane, numbered μ

$$\text{elastic regime: } \rho\frac{\partial U}{\partial \varepsilon_{N_\mu}} = w_\mu \rho\frac{\partial U_\mu}{\partial \varepsilon_{N_\mu}} = \sigma_{N_\mu} \tag{37}$$

$$\rho\frac{\partial U}{\partial \varepsilon_{T_\mu}} = w_\mu \rho\frac{\partial U_\mu}{\partial \varepsilon_{T_\mu}} = \sigma_{T_\mu} \tag{38}$$

$$\text{tensile damage: } \rho\frac{\partial \Pi}{\partial \varepsilon_{N_\mu}} = w_\mu \rho\frac{\partial \Pi_\mu}{\partial \varepsilon_{N_\mu}} = \sigma_{N_\mu} \tag{39}$$

$$\text{compressive damage: } \rho\frac{\partial \Psi(\varepsilon_{N_\mu}, \varepsilon_V)}{\partial \varepsilon_{N_\mu}} = w_\mu \rho\left[\frac{\partial \Psi_\mu(\varepsilon_{N_\mu})}{\partial \varepsilon_{N_\mu}}\right]_{\varepsilon_V}$$
$$+ \rho\frac{\partial \Psi_\mu(\varepsilon_V)}{\partial \varepsilon_V}\frac{\partial \varepsilon_V}{(\partial \varepsilon_{N_\mu})} \tag{40}$$

$$= \sigma_{D_\mu} + \rho\frac{\mathrm{d}\Psi_V(\varepsilon_V)}{\mathrm{d}\varepsilon_V}\frac{\partial}{\partial \varepsilon_{N_\mu}}\sum_{\nu}^{N_m} w_\nu \varepsilon_{N_\nu} \tag{41}$$

$$= \sigma_{D_\mu} + \rho w_\mu\frac{\mathrm{d}\Psi_V(\varepsilon_V)}{\mathrm{d}\varepsilon_V} = \sigma_{D_\mu} + \sigma_V \tag{42}$$

$$\text{frictional slip: } \rho\frac{\partial \Phi}{\partial \dot\varepsilon_{T_\mu}} = w_\mu \rho\frac{\partial \Phi_\mu}{\partial \dot\varepsilon_{T_\mu}} = \sigma_{T_\mu}(\sigma_{N_\mu}) \tag{43}$$

where Eq. (42) uses the fact that the volumetric strain may approximately be expressed as $\varepsilon_V = (\sum_\nu^{N_m} \varepsilon_{N_\nu})/N_m$ (which becomes exact for $N_m \to \infty$). In Eq. (43), $\sigma_{T_\mu}(\sigma_{N_\mu})$ is the microplane shear stress as a function of the microplane normal stress, which is a functional dependence that characterizes friction on the microplane. The mass density ρ appears in the foregoing equations, because the potentials are defined per unit mass whereas the stress is the energy per unit volume.

Alternatively, one could obtain the same result by considering the number of microplanes $N_m \to \infty$, which would convert the sums in the foregoing equations into integrals over Ω. But the differentiation with respect to the variables of one particular microplane would become trickier, as it would necessitate the use of Dirac delta functions of spherical angles. The discrete form in Eqs. (38)–(43) is simpler.

Eq. (35) reflects the fact that the microplane normal strain ε_{N_μ} does not suffice to characterize cracking damage and that the volume change is important, too. As shown by Eq. (42), this implies that, for characterizing the cracking damage, the normal microplane strain must inevitably be split into its volumetric and deviatoric parts, as stated in Eq. (4). Without this split it is impossible to capture the salient feature that unconfined (uniaxial or biaxial) compression and weakly confined compression produce postpeak softening, whereas highly confined compression and hydrostatic compression lead to no peak and no softening. So, the kind of compressive behavior depends on whether the volume growth is restricted.

However, by contrast to previous microplane models, it is important to note that the volumetric-deviatoric split of normal microplane strains is not required, and not useful, for the elastic regime and also the tensile cracking (damage) regime. This is reflected in potentials U and Π, which are functions of ε_{N_μ} only, and in Eqs. (37) and (39), which lead to normal stress without split. In the current study, such split has actually been found to harm the modeling power. So, in departure from microplane models M2, . . . , M6, the volumetric-deviatoric split for elastic strains and for tensile cracking is here abandoned.

Admittedly, the present formulation of potentials is unorthodox. It does not conform to the classical thermodynamics of continua, but it is simple and is convenient for dealing with separate stress-strain boundaries for different physical processes. The basic thermodynamic hypothesis that naturally leads to the microplane model is that the total potential density (or Helmholtz free energy density) at a point of the macroscopic continuum is the sum of the potentials associated with planes of deformation (or microplanes) of all possible orientations within the material ($\nu = 1, 2, . . . , N_m$), as postulated in Eqs. (37)–(43). However, a rigorous thermodynamic formulation based on this hypothesis has so far been fully worked out only for some simplistic microplane models with limited data-fitting capability. A rigorous and complete thermodynamic formulation of a realistic microplane model still remains an elusive goal. One purpose of this appendix is to provoke further debate.

Acknowledgments

References

Asaro, R. J., and Rice, J. R. (1977). "Strain localization in ductile single crystals." *J. Mech. Phys. Solids*, 25(5), 309–338.

Batdorf, S., and Budianski, B. (1949). "A mathematical theory of plasticity based on the concept of slip." *NACA Technical Note 1871*, National Advisory Committee for Aeronautics, Washington, DC.

Bažant, Z. (1984). "Microplane model for strain-controlled inelastic behavior." Chapter 3, *Mechanics of engineering materials*, C. S. Desai and R. H. Gallagher, eds., Wiley, London, 45–59.

Bažant, Z., and Gambarova, P. (1984). "Crack shear in concrete: Crack band microplane model." *J. Struct. Eng.*, 110(9), 2015–2035.

Bažant, Z., and Yu, Q. (2011). "Size effect testing of cohesive fracture parameters and non-uniqueness of work-of-fracture method." *J. Eng. Mech.*, 137(8), 580–588.

Bažant, Z. P. (2010). "Can multiscale-multiphysics methods predict softening damage and structural failure?" *Int. J. Multiscale Comput. Eng.*, 8(1), 61–67.

Bažant, Z. P., and Caner, F. C. (2005a). "Microplane model M5 with kinematic and static constraints for concrete fracture and anelasticity. I. Theory." *J. Eng. Mech.*, 131(1), 31–40.

Bažant, Z. P., and Caner, F. C. (2005b). "Microplane model M5 with kinematic and static constraints for concrete fracture and anelasticity. II. Computation." *J. Eng. Mech.*, 131(1), 41–47.

Bažant, Z. P., Caner, F. C., Carol, I., Adley, M. D., and Akers, S. A. (2000). "Microplane model M4 for concrete: I. Formulation with work-conjugate deviatoric stress." *J. Eng. Mech.*, 126(9), 944–953.

Bažant, Z. P., and Cedolin, L. (1991). *Stability of structures: Elastic, inelastic, fracture and damage theories*, Oxford University Press, New York.

Bažant, Z. P., Kim, J.-J. H., and Brocca, M. (1999). "Finite strain tube-squash test of concrete at high pressures and shear angles up to 70 degrees." *ACI Mater. J.*, 96(5), 580–592.

Bažant, Z. P., and Oh, B.-H. (1983). "Microplane model for fracture analysis of concrete structures." *Proc., Symp. on the Interaction of Non-Nuclear Munitions with Structures*, U.S. Air Force Academy, Colorado Springs, CO, 49–53.

Bažant, Z. P., and Oh, B.-H. (1985). "Microplane model for progressive fracture of concrete and rock." *J. Eng. Mech.*, 111(4), 559–582.

Bažant, Z. P., and Oh, B.-H. (1986). "Efficient numerical integration on the surface of a sphere." *Z. Angew. Math. Mech.*, 66(1), 37–49.

Bažant, Z. P., and Prat, P. C. (1988a). "Microplane model for brittle plastic material: I. Theory." *J. Eng. Mech.*, 114(10), 1672–1688.

Bažant, Z. P., and Prat, P. C. (1988b). "Microplane model for brittle plastic material: II. Verification." *J. Eng. Mech.*, 114(10), 1689–1702.

Bažant, Z. P., Wu, J.-Y., Caner, F. C., and Cusatis, G. (2010). "How to enforce non-negative energy dissipation in microplane and other constitutive models of softening damage, plasticity and friction." *Computational Modeling of Concrete Structures, Proc., EURO-C Conf.*, Taylor & Francis, London, 87–91.

Bažant, Z. P., Xiang, Y., and Prat, P. C. (1996). "Microplane model for concrete. I. Stress-strain boundaries and finite strain." *J. Eng. Mech.*, 122(3), 245–254.

Brocca, M., and Bažant, Z. P. (2000). "Microplane constitutive model and metal plasticity." *Appl. Mech. Rev.*, 53(10), 265–281.

Butler, G. C., and McDowell, D. L. (1998). "Polycrystal constraint and grain subdivision." *Int. J. Plast.*, 14(8), 703–717.

Caner, F. C., and Bažant, Z. P. (2000). "Microplane model M4 for concrete. II: Algorithm and calibration." *J. Eng. Mech.*, 126(9), 954–961.

Caner, F. C., and Bažant, Z. P. (2002). "Lateral confinement needed to suppress softening of concrete in compression." *J. Eng. Mech.*, 128(12), 1304–1313.

Caner, F. C., and Bažant, Z. P. (2011). "Microplane model M6f for fiber reinforced concrete." *Proc., XI Int. Conf. on Computational Plasticity Fundamentals and Applications, COMPLAS 2011*, D. P. E. Oñate, D. R. J. Owen, and B. Suárez, eds., Centro Internacional de Métodos Numéricos en Ingeniería, Univ. Politècnica de Catalunya, Barcelona, Spain, 796–807.

Caner, F. C., and Bažant, Z. P. (2013). "Microplane model M7 for plain concrete. II: Calibration and verification." *J. Eng. Mech.*, 139(12), 1724–1735.

Caner, F. C., Bažant, Z. P., and Červenka, J. (2002). "Vertex effect in strain-softening concrete at rotating principal axes." *J. Eng. Mech.*, 128(1), 24–33.

Caner, F. C., Bažant, Z. P., Hoover, C., Waas, A., and Shahwan, K. (2011). "Microplane model for fracturing damage of triaxially braided fiber-polymer composites." *J. Eng. Mater. Technol.*, 133(2), 021024.

Carol, I., and Bažant, Z. P. (1997). "Damage and plasticity in microplane theory." *Int. J. Solids Struct.*, 34(29), 3807–3835.

Carol, I., Jirásek, M., and Bažant, Z. P. (2001). "A thermodynamically consistent approach to microplane theory. Part I. Free energy and consistent microplane stresses." *Int. J. Solids Struct.*, 38(17), 2921–2931.

Cusatis, G., Bažant, Z. P., and Cedolin, L. (2003). "Confinement–shear lattice model for concrete damage in tension and compression: I. Theory." *J. Eng. Mech.*, 129(12), 1439–1448.

Cusatis, G., Beghini, H., and Bažant, Z. P. (2008). "Spectral stiffness microplane model for quasibrittle composite laminates—Part I: Theory." *J. Appl. Mech.*, 75(2), 021009.

Cusatis, G., Mencarelli, A., Pelessone, D., and Baylot, J. T. (2011a). "Lattice discrete particle model (LDPM) for failure behavior of concrete. II: Calibration and validation." *Cement Concr. Compos.*, 33(9), 891–905.

Cusatis, G., Pelessone, D., and Mencarelli, A. (2011b). "Lattice discrete particle model (LDPM) for failure behavior of concrete. I: Theory." *Cement Concr. Compos.*, 33(9), 881–890.

Fung, Y. C. (1968). *Foundations of solid mechanics*, Prentice Hall, Englewood Cliffs, NJ.

Hasegawa, T., and Bažant, Z. P. (1993a). "Nonlocal microplane concrete model with rate effect and load cycles. I: General formulation." *J. Mater. Civ. Eng.*, 5(3), 372–410.

Hasegawa, T., and Bažant, Z. P. (1993b). "Nonlocal microplane concrete model with rate effect and load cycles. II: Application and verification." *J. Mater. Civ. Eng.*, 5(3), 394–410.

Hill, R., and Rice, J. R. (1972). "Constitutive analysis of elastic-plastic crystal at arbitrary strain." *J. Mech. Phys. Solids*, 20(6), 401–413.

Jirásek, M., and Bažant, Z. P. (2002). *Inelastic analysis of structures*, Wiley, London.

Rice, J. (1971). "Inelastic constitutive relations for solids: An internal variable theory and its application to metal plasticity." *J. Mech. Phys. Solids*, 19(6), 433–455.

Stroud, A. H. (1971). *Approximate calculation of multiple integrals*, Prentice Hall, Englewood Cliffs, NJ.

Corrections

Erratum for "Microplane Model M7 for Plain Concrete. I: Formulation" by Ferhun C. Caner and Zdeněk P. Bažant

Ferhun C. Caner, Aff.M.ASCE

Associate Professor, Institute of Energy Technologies, Barcelona School of Industrial Engineering, Universitat Politècnica de Catalunya, Campus Sud, 08028 Barcelona, Spain.

Zdeněk P. Bažant, Hon.M.ASCE

Distinguished McCormick Institute Professor and W. P. Murphy Professor of Civil Engineering, Mechanical Engineering, and Materials Science, Dept. of Civil and Environmental Engineering, Northwestern Univ., Evanston, IL 60208 (corresponding author). E-mail: z-bazant@northwestern.edu

The following corrections should be made.

Replace Eq. (14) with

$$\alpha = \frac{k_5}{1 + \min(\langle -\sigma_V^0 \rangle, c_{21})/E_{N0}} \left(\frac{\varepsilon_I^0 - \varepsilon_{III}^0}{k_1} \right)^{c_{20}} + k_4$$

where $c_{21} = 250\,\text{MPa}$.

Replace Eq. (23) with

$$\sigma_N^b = Ek_1\beta_1 e^{-\langle \varepsilon_N - \beta_1 c_2 k_1 \rangle / [c_4 \varepsilon_e + k_1 c_3]}$$

where $\beta_1 = -c_1 + c_{17} e^{-c_{19}\langle -\sigma_V^0 - c_{18} \rangle / E_{N0}}$ in which $c_{18} = 62.5\,\text{MPa}$.

Replace Eq. (26) with

$$\hat{\sigma}_N^0 = E_T \langle k_1 c_{11} - c_{12} \langle \varepsilon_V \rangle \rangle$$

The element deletion criterion was specified as $\varepsilon_I \geq 0.5\%$.

Microplane Model M7 for Plain Concrete. II: Calibration and Verification

Ferhun C. Caner[1] and Zdeněk P. Bažant, Hon.M.ASCE[2]

Abstract: The microplane material model for concrete, formulated mathematically in the companion paper, is calibrated by material test data from all the typical laboratory tests taken from the literature. Then, the model is verified by finite-element simulations of data for some characteristic tests with highly nonuniform strain fields. The scaling properties of model M7 are determined. With the volumetric stress effect taken from the previous load step, the M7 numerical algorithm is explicit, delivering in each load step the stress tensor from the strain tensor with no iterative loop. This makes the model robust and suitable for large-scale finite-element computations. There are five free, easily adjustable material parameters, which make it possible to match the given compressive strength, the corresponding strain, the given hydrostatic compression curve, and certain triaxial aspects. In addition, there are many fixed, hard-to-adjust parameters, which can be taken to be the same for all concretes. The optimum values of material parameters are determined by fitting a particularly broad range of test results, including the important tests of compression-tension load cycles, mixed-mode fracture, tension-shear failure of double-edge-notched specimens, and vertex effect when axial compression is followed by torsion. Because of the lack of information on the material characteristic length or fracture energy, which can be obtained only by size effect tests on the same concrete, and on the precise boundary conditions and precise gauge locations, the finite-element fitting of the present test data can hardly be expected to give better results than single-point simulations of specimens with approximately homogeneous strain states within the gauge length. Nevertheless, tensile test data with severe localization are delocalized on the basis of assumed material length. Model M7 is shown to fit a considerably broader range of test data than the preceding models M1–M6. **DOI:** 10.1061/(ASCE)EM.1943-7889.0000571. *© 2013 American Society of Civil Engineers.*

CE Database subject headings: Constitutive models; Inelasticity; Cracking; Damage; Concrete; Experimentation; Verification; Data processing; Calibration; Finite element method.

Author keywords: Constitutive modeling; Inelastic behavior; Cracking damage; Concrete; Experimental verification; Data fitting; Model calibration; Finite-element analysis.

Introduction

As a sequel to the theoretical formulation in the companion paper (Caner and Bažant 2013) of this study, the present paper deals with the calibration of microplane model M7 and its verification by laboratory test data from the literature. All the definitions and notations are retained.

Obstacles to Inverse Finite-Element Analysis of Tests with Postpeak Softening

Optimal identification of material parameters by inverse finite-element analysis of experimental data with softening faces certain obstacles. When postpeak softening takes place, either the crack band model or the nonlocal model must be used to suppress spurious mesh sensitivity. In either case, one must know the material characteristic length l_0 or the reference element size h_0 for the crack band model. It used to be thought that h_0 were equal to about the double of the maximum aggregate size d_a, but now it is understood that the ratio h_0/d_a can vary significantly, depending on other properties of concrete.

The only way to determine l_0 or h_0 experimentally is to conduct notched fracture tests of specimens with significantly different sizes made from the same batch of concrete. Recently, it has been shown that the load-deflection curve with complete postpeak softening can be fitted by using l_0-values or tensile strength values that differ by 70% and that unique results are obtained when the load-deflection curves are tested on specimens of significantly different specimen sizes (Bažant and Yu 2011). Likewise, when finite elements of different sizes are used, the crack band simulation of the softening parts of the present data can lead to very different model calibrations.

Unfortunately, for the triaxial test data in the literature, no experimental information on l_0 or h_0 exists. Therefore, inverse finite-element analysis of the softening part of the test data considered here is inevitably ambiguous.

Another obstacle to meaningful inverse finite-element analysis is the insufficiency of information about the precise boundary conditions of the test specimens and the precise location of the gauges on the specimens. Consequently, single-point simulations, with some delocalization of softening, are pursued here as the main approach for material parameter calibration. Nevertheless, finite-element

[1] Associate Professor, Institute of Energy Technologies, School of Industrial Engineering, Univ. Politecnica de Catalunya, Campus Sud, 08028 Barcelona, Spain; presently, Visiting Scholar, Dept. of Civil and Environmental Engineering, Northwestern Univ., Evanston, IL 60208. E-mail: ferhun.caner@upc.edu

[2] Distinguished McCormick Institute Professor and W. P. Murphy Professor of Civil Engineering, Mechanical Engineering, and Materials Science, Northwestern Univ., Evanston, IL 60208 (corresponding author). E-mail: z-bazant@northwestern.edu

analysis of some test specimens is subsequently used to check that the fits are reasonable.

The best estimate l_0 could in theory be obtained by simulation of fracture tests of each given concrete with the lattice-particle model (Cusatis et al. 2003, 2011a, b). However, this is a demanding task that requires further study and is beyond the scope of a single paper.

Even if the aforementioned obstacles did not exist, it would be difficult to begin with finite-element fitting, because often an incorrect initial guess of material parameters is made, which then leads to convergence problems at worst and excessively long run times at best. In addition, the simulation of fracturing may easily be corrupted by mesh bias, which favors fractures running along the mesh lines, and by numerical problems such as stress locking, which may give rise to spurious crack paths (Jirásek and Zimmermann 1998).

It has been checked that the spurious mesh sensitivity and mesh dependence of energy dissipated by localized fracture can be avoided if the normal tensile boundary and the deviatoric compression boundary are scaled horizontally according to the element size, as required by the crack band model (Bažant and Oh 1983). The scaling represents an affinity transformation with respect to the elastic line as the affinity axis [Bažant and Caner 2005, Fig. 1 (left)]

Calibration of Model M7 Assuming Homogeneous Strain Field

The main assumption in single-point simulations is that the zone spanned by the gauge is deformed nearly homogeneously and lies far enough from boundary disturbances. Tensile softening, however, is an exception in which the strain gets localized so severely that the test data must at least be approximately delocalized, as described in Bažant et al. (1996). The postpeak compression, too, is subjected to localization, but the localization zone is often as large as the gauge length, and so, the single-point simulation should suffice. In certain important cases, the single-point fitting will nevertheless be followed by finite-element analysis with the crack band model using a judiciously assumed reference size h_0.

When only a few types of tests of concrete are used for calibration, many different models can fit the same data. Therefore, all the known basic types of laboratory tests are considered here to verify and calibrate model M7. Omitting some of them would lead to ambiguity. The optimized fits of material data by model M7 using a single material point are presented first. Subsequently, the parameter values from these fits are used to analyze various problems by finite elements, using the crack band model with element size roughly equal to d_a. (The element sizes used in the simulations are obvious from the figures, but they are also reported along with the model free parameters used in the analyses.)

Two types of data are fitted: (1) data coming from different laboratories, obtained by different researchers using different concretes (Figs. 1 and 2); and (2) data coming from the same laboratory, obtained by the same researchers using one and the same concrete (Fig. 3). Because the responses of concrete to various triaxial loading histories are very different, many different kinds of tests have to be fitted to achieve unique calibration.

Some of the data fitted in this study have previously also been fitted by models M3, M4, M5, and M6. They constitute the classical benchmark data. In this paper, the authors enlarge the benchmark data set by fitting some characteristic data that have not been fitted before. The values of the adjustable (or variable) parameters of model M7 corresponding to each fit shown are given in each figure, along with a reference to the data source. Because the fixed material parameters are common to all the figures, they are shown only in Table 1.

The adjustable parameters, denoted as k_I ($I = 1, 2, \ldots, 5$), have increased in number from four in microplane models M4–M6 to five in the present model M7, as shown in Table 2. The main reason for this increase is to introduce a refined volumetric-deviatoric coupling with a twofold aim: (1) to simulate data through the entire range from low-strength to normal-strength concretes and (2) to capture the dilatation attributable to shear, called the dilatancy, which may be more pronounced in some concretes than others. For normal-strength concretes, the interactions among the microplanes suffice to automatically reproduce the dilatancy. But in concretes of relatively low strength, they do not. The dilatancy of such concretes can be simulated only through an explicit dependence of the deviatoric behavior on the volumetric strain and vice versa, a coupling that is allowed by M7. In the preceding microplane models, it was virtually impossible to fit the triaxial compression data for lower-strength concretes, which exhibit a particularly strong dilatancy under shear.

Fig. 1(a) demonstrates an excellent fit of the uniaxial compression test data from van Mier (1986a, b). (In all figures, the values measured in the tests are shown by circles, and the curves are the model predictions.) Though not visible in the figure, the response for large compressive strains monotonically decreases to zero and then remains zero. Such behavior was not achieved in the earlier versions of the microplane models for concrete.

Fig. 1(b) shows a reasonably good fit of test data of van Mier (1984) for the volume expansion of concrete under uniaxial compression. A close fit of the peak region of the data could not be achieved, but the postpeak expansion has been captured well.

Fig. 1(c) depicts the triaxial test data from Balmer (1949) and their fit by model M7. For both higher and lower confinement values, the fits are very accurate, better than with the preceding microplane models.

Fig. 1(d) presents a biaxial failure envelope reported in Kupfer et al. (1969) and its excellent simulation by model M7. One of the main advantages of model M7 is its improved capability to simulate the biaxial compressive behavior, which is important for applications to plates, membranes, and shells. The current model is exceptionally well suited for the multiaxial behavior of such structural members.

Fig. 1(e) shows the data on the shear-compression failure envelope measured by Bresler and Pister (1958). They are fitted by model M7 very well, better than by the previous microplane models for concrete. This improvement is important for finite-element analysis of columns, beams, plates, and shells.

Fig. 1(f) shows the test data for confined compression of cement paste from Bažant et al. (1986) and their excellent fit achieved by model M7. Very high pressures have been obtained in these tests. The previous microplane models could fit these data just as well but could not differentiate between the hydrostatic compression and the confined compression at zero lateral strain.

Fig. 1(g) depicts test data for hydrostatic compression from Green and Swanson (1973), in which the stresses are normalized by the compressive strength, and their fits by model M7. Note that the fit is excellent for both the loading and unloading regimes. Compared with its predecessors, model M7 predicts the unloading better.

Fig. 1(h) presents uniaxial tension test data from Petersson (1981) for two different concretes and their fits by model M7. The lateral contraction response predicted by model M7 appears to the left of the origin. There seems to be no experimental data for the lateral contraction under uniaxial tensile loading, probably because the deformation localizes into a very small zone, the location of which cannot be known in advance. However, in the sense of the macrocontinuum model pursued now, a large extension causes the material to become intersected by a series of parallel densely distributed cracks, leaving stress-free material between the cracks.
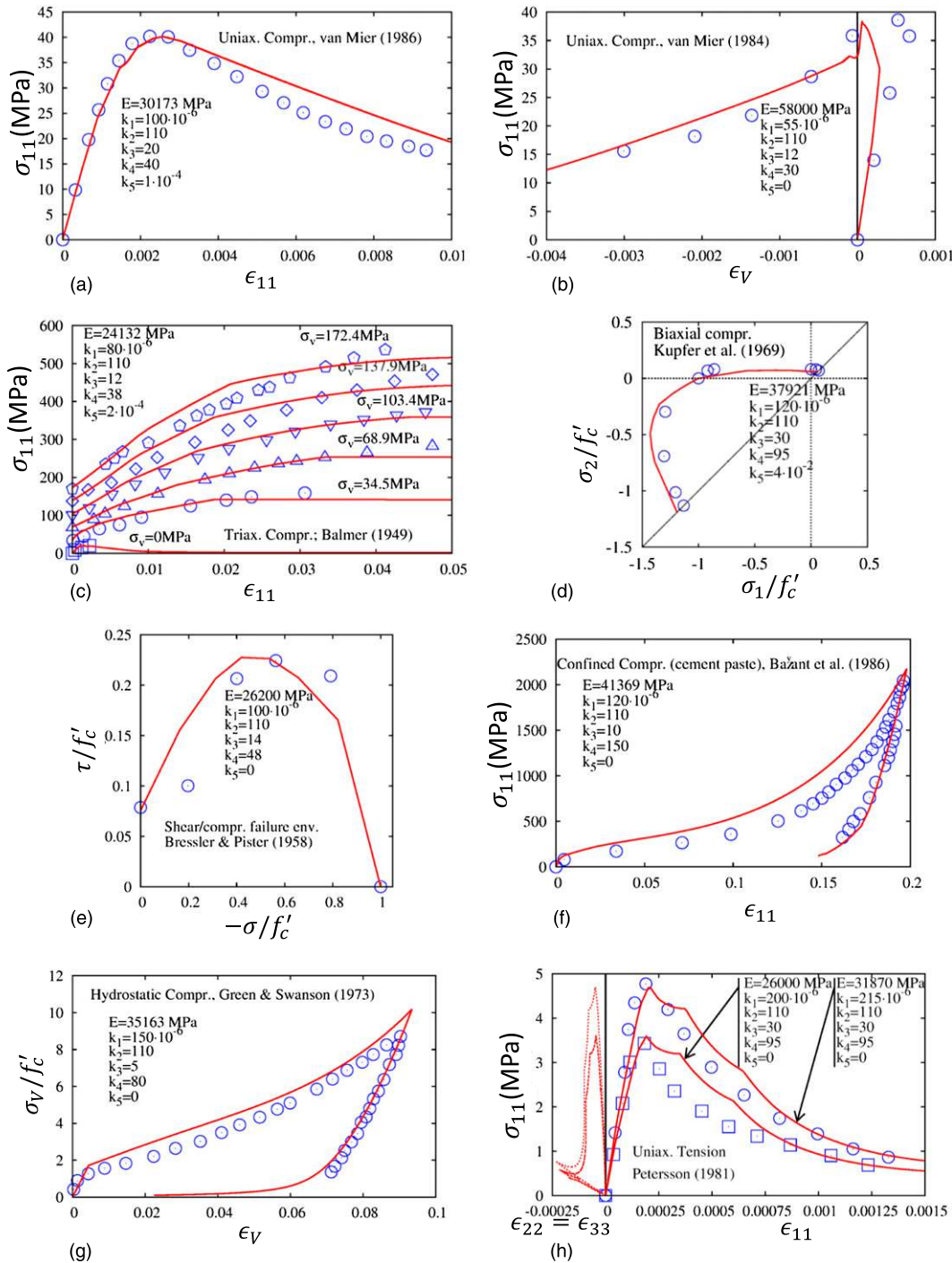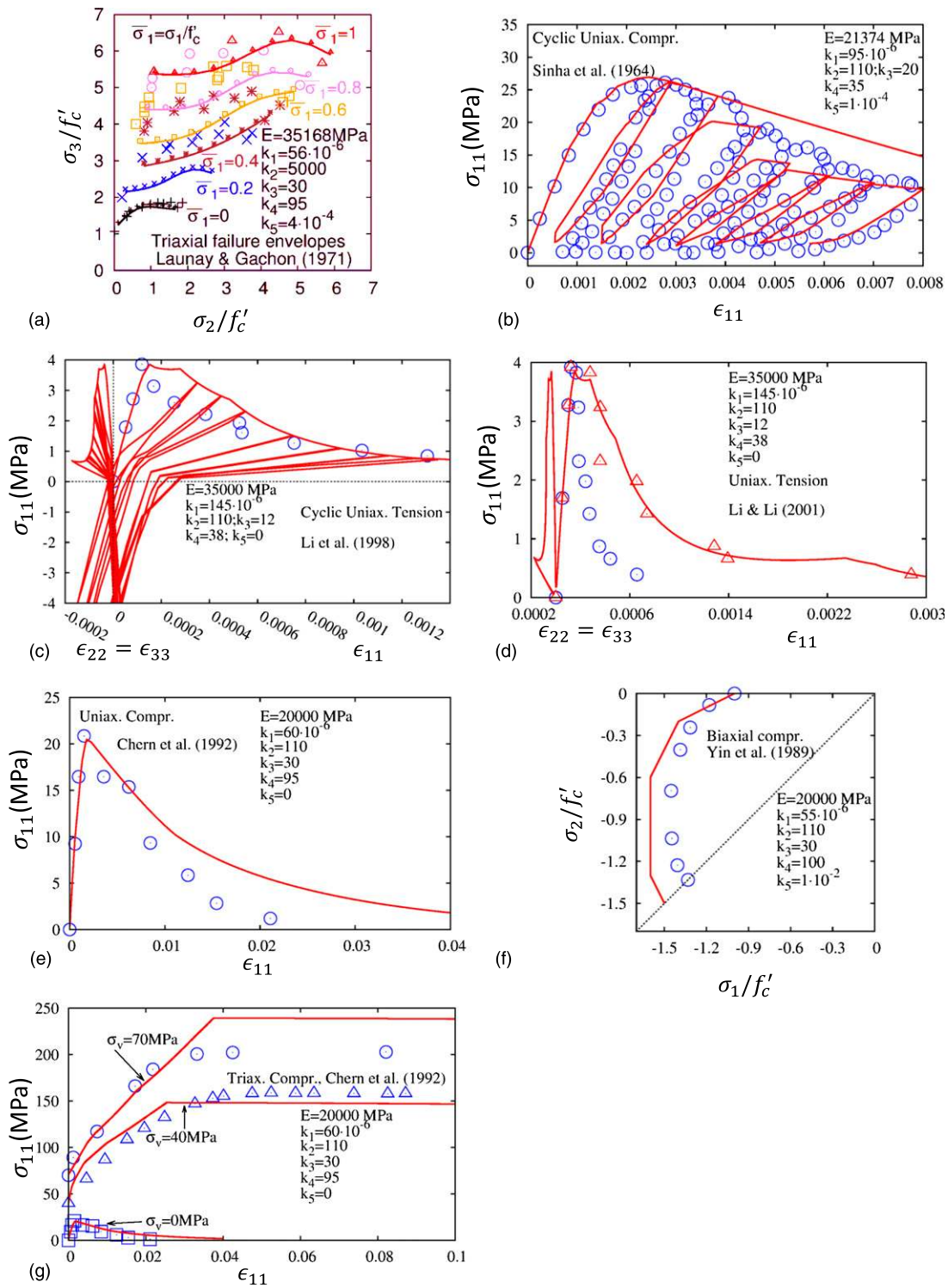
Fig. 1. First part of benchmark data set for different concretes, used to evaluate the model and optimize material parameters

Therefore, in a continuum model, the lateral contraction must approach zero as the axial stress gets reduced to zero in the far postpeak tail of the uniaxial tension curve.

The current model automatically captures this behavior, whereas its predecessors M3 and M4 could not capture it at all because of the volumetric-deviatoric split of elastic strains. Models M5 and M6 were able to simulate this behavior by means of a smooth transition from a split to a no-split formulation during tensile softening. But this transition makes impossible a good modeling of the unloading and cyclic loading, turns out not to be robust in large-scale computations, and does not have a general applicability. For example, it runs into a conflict when the material is in postpeak tension in the

x-direction, which requires no split, and simultaneously in postpeak compression in the y-direction, which requires the split. With the current model, the problem of spurious lateral contraction under uniaxial tension is totally eliminated, and this is achieved in a continuous and robust manner, without the use of any potentially troublesome transitions.

Fig. 2 presents the set of basic benchmark data and their single-point material fits by the current model. Fig. 2(a) shows the M7 fits of test data from Launay and Gachon (1971) in the form of triaxial failure envelopes in which the stresses are normalized by the compressive strength of concrete. These data are obtained by prescribing a loading path in three dimensions (3D) in which the applied

Fig. 2. Second part of the benchmark data set for different concretes, used to evaluate the model and optimize material parameters

stress in one direction ($\overline{\sigma}_1$) is fixed to a value (e.g., 0.2), and then, the specimen is loaded to failure in the remaining two directions following various load paths in two dimensions (in the σ_2, σ_3-plane). In a previous work (Bažant et al. 1996), these data and the simulation results (by model M3) were plotted in the octahedral plane, which led to an apparently poor fit of these data.

However, it must be noted that, while the simulations can be carried out (though with great difficulties) for a few load paths so as to create failure envelopes for apparently constant pressure, the tests

actually cannot be performed for a constant pressure at the moment of failure. As a result, the octahedral plot is not fully meaningful for data fitting. Therefore, this study fits model M7 to the data points in a two-dimensional (2D) graph, as originally plotted by the experimenters Launay and Gachon (1971).

Along the path $\sigma_2 = \sigma_3$, the model prediction for the strength of concrete is excellent for all confinement levels except $\overline{\sigma}_1 = 0.4$. For other nonproportional paths, the M7 predictions of strength are consistently lower than the experimental values. They appear to be
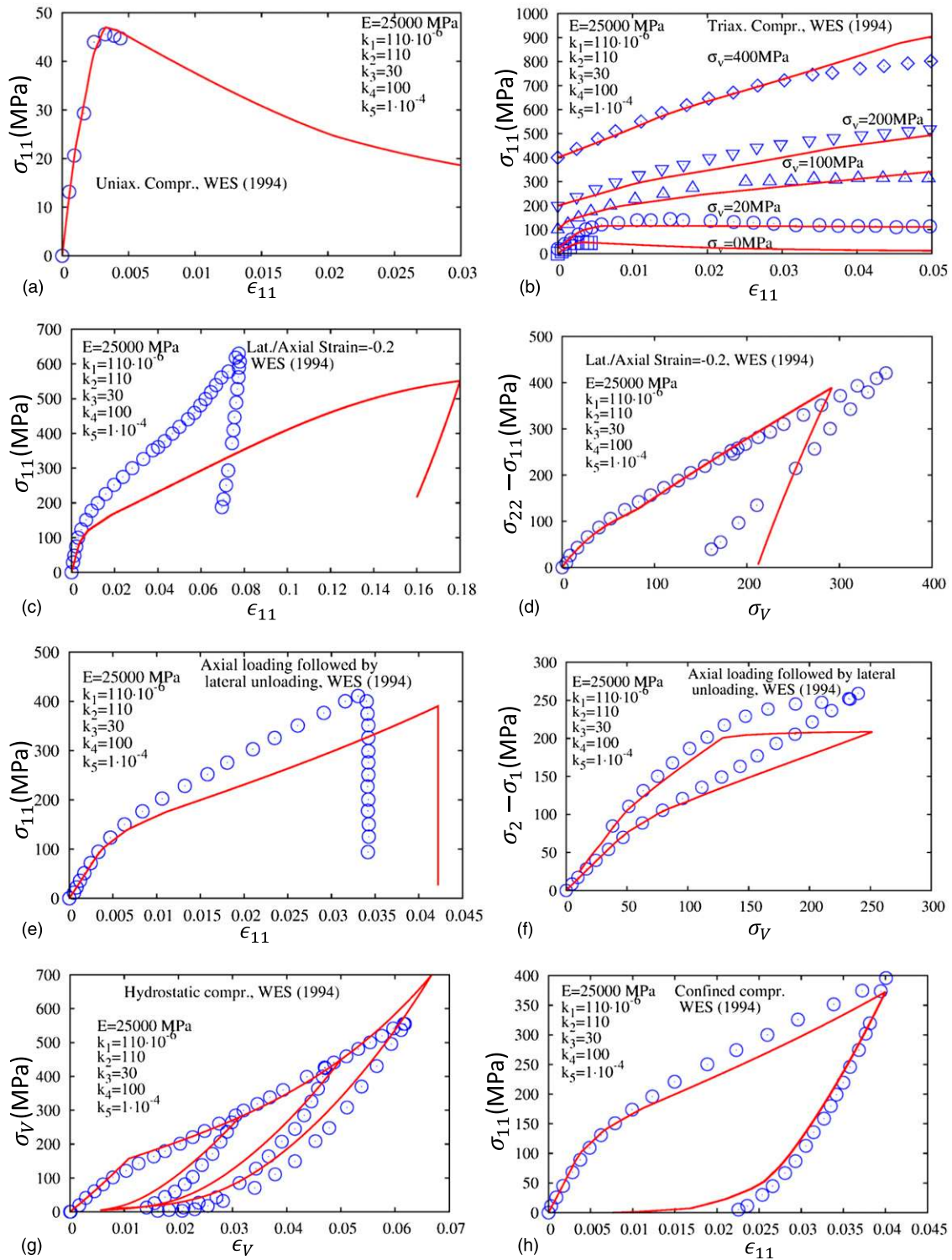
Fig. 3. Benchmark set of test data obtained with one and the same concrete, used to evaluate the model and optimize material parameters

better for the triaxial strength values under high confinement, as is generally the case for all microplane models. These tests have proven to be difficult to simulate with the microplane and other models in general. The performance of model M7 is by far the best among all microplane models for concrete.

Fig. 2(b) depicts cyclic uniaxial compression data from Sinha et al. (1964) and their fit by the model M7. The envelope of the cyclic data plotted in the figure is predicted as well. The areas of the predicted hysteretic loops, which represent the dissipated energy,

agree with the experiments. The loading and unloading slopes are also in agreement with the experimental loading and unloading slopes in both the compressive and tensile regions. In contrast to M3, M4, M5, and M6, model M7 delivers consecutive hysteretic loops with a progressively decreasing strength limit, which is an essential aspect of fatigue.

To provide a comparison of the single-point simulation to the finite-element modeling of similar uniaxial tension test data, Fig. 2(c) shows the test data by Li et al. (1998) and simulations for postpeak

Table 1. Fixed Parameters of the Model M7, Their Typical Values, and Their Meanings

Parameter	Value	Meaning
f_{c0}'	15.08 MPa	Reference compressive strength
E_0	20 GPa	Reference elastic modulus
c_1	$8.9 \cdot 10^{-2}$	Controls the uniaxial tensile strength
c_2	$17.6 \cdot 10^{-2}$	Controls the roundness of the peak in uniaxial tension
c_3	4	Controls the slope of the postpeak in uniaxial tension
c_4	50	Controls the slope of the postpeak tail in uniaxial compression
c_5	3,500	Controls the volumetric expansion under compression
c_6	20	Controls the roundness of the peak in volumetric expansion under compression
c_7	1	Controls the slope of the initial postpeak in uniaxial compression
c_8	8	Controls the peak strength in uniaxial compression
c_9	$1.2 \cdot 10^{-2}$	Controls the peak roundness in uniaxial compression
c_{10}	0.33	Controls the effective friction coefficient
c_{11}	0.5	Initial cohesion in frictional response
c_{12}	2.36	Controls the change of cohesion with tensile volumetric strains
c_{13}	4,500	Controls the unloading slope in tension
c_{14}	300	Controls the unloading slope at low hydrostatic compression
c_{15}	4,000	Controls the transition from unloading slope at high confinement to that at low confinement
c_{16}	60	Controls the unloading slope at high hydrostatic compression
c_{17}	1.4	Controls the tensile strength
c_{18}	$1.6 \cdot 10^{-3}$	Controls the tensile cracking under compression
c_{19}	1,000	Controls the tensile softening rate induced by compression
c_{20}	1.8	Controls the volumetric-deviatoric coupling at high pressures

Table 2. Free Parameters of the Model M7, Their Typical (or Default) Values, and Their Meanings

Parameter	Value	Meaning
E	25,000 MPa	Elastic modulus (and vertical scaling parameter)
ν	0.18	Poisson's ratio
k_1	$1.5 \cdot 10^{-4}$	Radial scaling parameter
k_2	110	Controls the horizontal asymptote value in the frictional boundary
k_3	30	Controls the shape of the volumetric boundary
k_4	100	Controls the shape of the volumetric boundary
k_5	$1 \cdot 10^{-4}$	Controls the volumetric-deviatoric coupling at low pressures

uniaxial tension and tension-compression load cycles. The effect of the load cycles on the lateral contraction is seen to the left of the origin. To the right of the origin, the load cycles shown give a comparison of this single-point simulation to a finite-element simulation of similar uniaxial tension test data presented in the "Finite-Element Verification of M7 on Specimens with Non-homogeneous Strain Field" section (Fig. 4). The effect of the load cycles on the lateral contraction is seen to the left of the origin (where the horizontal coordinate axis serves as the transverse strain coordinate).
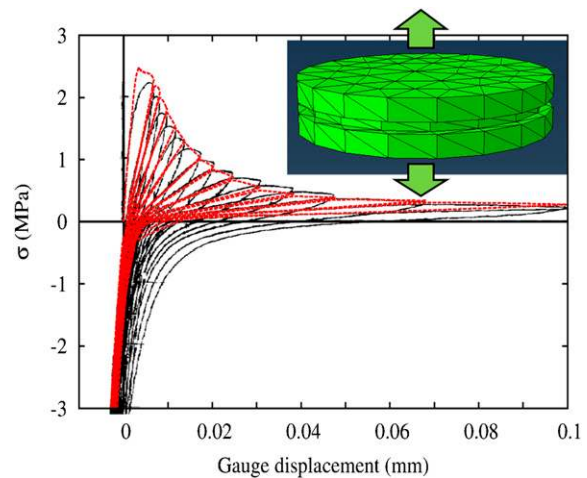
Fig. 4. Finite-element simulations of compression-tension load cycles in which test data are from Reinhardt and Cornelissen (1984)

Note that, for very large axial strains, the lateral contraction gradually relaxes to zero.

Fig. 2(d) displays by circles the test data for uniaxial tension reported in Li and Li (2000), by triangles the data obtained by delocalizing this original data, and by a continuous curve their simulation with model M7. The parameter set used in the simulation is identical to that in Fig. 2(c), and in both Figs. 2(c and d), the data correspond to the same elastic modulus and the same strength. Yet, the data compare very differently to the same simulation in these two figures. These figures are included specifically to emphasize an important difference between the test data and the model predictions that may result from unloading within the gauge span in the tensile specimens. If the gauge span is long, crack formation causes the surrounding material to unload, which produces a sharp drop in the postpeak stress-strain curve. In this particular simulation, finite-element analysis is obviously better for parameter optimization than the analysis at a single material point. (These data are not fitted using the FEM, because similar data are already fitted in Fig. 4.)

Fig. 2(e) depicts test data for uniaxial compression of a lower-strength concrete ($f_c' = 21$ MPa) as reported in Chern et al. (1992) and their fit by model M7, which is seen to be excellent. Lower-strength concretes exhibit larger dilatancy under shear than normal-strength concretes do. The predecessors of model M7 could not capture such large dilatancy, because they lacked an explicit dependence of the volumetric response on the deviatoric strains.

Fig. 2(f) shows the biaxial test data from Yin et al. (1989) and their fit by model M7. The fit is reasonably good. Other biaxial data, which are fitted better than before, appear in Figs. 1(d) and 2(a). (Notice the curve that corresponds to $\overline{\sigma}_1 = 0$.)

Fig. 2(g) shows the test data for triaxial compression of a lower-strength concrete reported in Chern et al. (1992) and their fits by model M7 using the same parameter set as shown in the figure. By virtue of the explicit dependence of the volumetric response on the deviatoric strains, the fits are reasonably good. Note that the preceding microplane models could not fit these data at all.

Fig. 3 compares model M7 to the set of data from various conventional and unconventional tests conducted by the U.S. Army Engineers Waterways Experiment Station (WES) in 1994 and reported in Bažant et al. (1996). All the tests were done at one time, in the same laboratory, and with one and the same concrete (i.e., with the same mix design and the same aggregates). This set of data

represents a tougher check on the present model, because all the model parameters must be the same for all these tests.

Fig. 3(a) depicts the uniaxial compression test results and their fit by model M7. The fit is good. Fig. 3(b) shows the triaxial compression test data for various confining pressures and their fits, which are again good. Fig. 3(c) presents the test data obtained using a load path in which the lateral-to-axial strain ratio is enforced to be −0.2 and the comparison with the current model. This comparison is less than satisfactory, but it must be judged in view of the fact that the parameter set had to be kept constant for all the figures. Thus, what matters is whether a major part of all the test data in this set could be fitted satisfactorily.

Fig. 3(d) shows, for the same load path, the plot of the principal stress difference versus the volumetric stress. Here the prediction is good. Fig. 3(e) depicts the test data for axial compression followed by lateral unloading and their fit by model M7. The fit is reasonably good. Fig. 3(f) shows the test data for the principal stress difference versus the volumetric stress and reveals a good fit.

Fig. 3(g) presents the monotonic and cyclic hydrostatic compression test data. Their simulation by model M7 is again seen to be good. Lastly, Fig. 3(h) shows the fits of the test data for a confined compression test for both loading and unloading. Their fits are again good.

Overall, in the entire WES data set, optimally fitted with the same material parameters, there is only one data fit, the one shown in Fig. 3(c), which falls short of acceptability. All the others are either good or excellent. This is an outstanding performance compared with other models. It should also be noted that, even with expert attention, the results of experiments exhibit random scatter, which is particularly pronounced for a disordered material such as concrete. Given that the data in Fig. 3(c) represent a single test, rather than an average of several repeated tests, it is not impossible that this test may be a statistical outlier in which something went wrong. Moreover, note that the current fit could be improved if some of the fixed parameters were converted to free parameters. However, it is desirable to keep the number of free parameters as low as possible.

Finite-Element Verification of M7 on Specimens with Nonhomogeneous Strain Field

The finite-element results for selected characteristic experiments published in the literature are now presented. All the results were obtained using the commercial software *ABAQUS*, in which model M7 was coded as a VUMAT user material subroutine. The integration over the microplanes uses the 37-point optimal Gaussian integration formula [derived in Bažant and Oh (1986)], which is of 13th degree. (The accuracy of the previously used 21- and 28-point formulas was found to be insufficient for far-postpeak softening.)

The elements are quadratic tetrahedra oriented randomly so that the mesh bias can be minimized. The mesh is random to minimize the directional bias of failure surfaces. To avoid spurious mesh sensitivity, all the finite-element simulations are carried out in the sense of the crack band model, using a mesh size corresponding to the representative volume element of concrete, the size of which is given in what follows along with the model free parameters in the discussion of each analysis.

The first problem is the uniaxial compression-tension cycles reaching the strength limit in uniaxial tension. Fig. 4 shows such cycles simulated by model M7 as the solid curves superposed on the dashed curves representing the test data reported in Reinhardt and Cornelissen (1984). Unlike the data fitted in the other figures, the test data are not represented by discrete data points, because the crowded curves would be hard to distinguish as well as difficult to digitize accurately. The specimen analyzed and the finite-element mesh are shown in the figure. The specimen is a concrete cylinder with a circumferential notch 5 mm deep and 5 mm wide. The gauge length, which is 25 mm, is taken as the length of the whole cylinder to simplify the finite-element analysis. The diameter of the cylinder is 120 mm. The maximum aggregate size of the concrete was 16 mm. The analysis is again carried out in the sense of the crack band model. During the simulations, it is observed that the crack localizes in the plane of the notch.

Clearly, the discrepancy between the test data and the simulation is quite small and is appreciable only in the transition from tension to compression. The predicted response is perfectly continuous. The slopes of calculated loading and unloading match almost perfectly the slopes of the experimental curves. The free model parameters used to obtain the prediction curve are $E = 25{,}000$ MPa, $k_1 = 110 \cdot 10^{-6}$, $k_2 = 110$, $k_3 = 30$, $k_4 = 100$, and $k_5 = 1 \cdot 10^{-4}$. The finite-element size is taken to be 5 mm.

The second and third problems to be analyzed by finite elements are the tests of three-point-bend beams with an asymmetrical notch reported in Gálvez et al. (1998). In the second problem, designated as Type 1 [Gálvez et al. 1998, Fig. 2(a)], the beam, made from concrete with a maximum aggregate size of only 5 mm, had depth $D = 75$ mm, width $B = 50$ mm, and length $L = 340$ mm. The notch, of width 2 mm, reached to a depth of $0.5D$ and was located at distances of 37.5 mm from the left support and 150 mm from the right support. The load was applied at a distance of 84.98 mm to the right of the notch. This loading produced combined normal and shear stresses in the vertical crack-tip cross section and thus led to mixed-mode crack propagation. The mixed mode has perennially been a challenging problem, beyond the capability of many previous models. The simulations for both of these two problems were carried out using the free model parameters $E = 38{,}000$ MPa, $k_1 = 110 \cdot 10^{-6}$, $k_2 = 110$, $k_3 = 30$, $k_4 = 100$, and $k_5 = 1 \cdot 10^{-4}$. The finite-element size in this problem is taken to be 5 mm.

Fig. 5(a) portrays the experimentally observed crack pattern superimposed on the finite-element mesh. The evolving crack is indicated by darkened elements.

The experimentally observed range of the load versus the load-point displacement is shown in Fig. 5(b) as the shaded region between the gray curves. The solid curve is the model prediction. Clearly, a very good agreement with the experimentally observed crack path is achieved. The load-deflection diagram agrees with the test data reasonably well.

The third problem is the test designated in Gálvez et al. (1998) as Type 2. In this test, a much higher shear stress in the crack-tip cross section is achieved by controlling the displacement at the free end of the beam, whose dimensions are the same as in the aforementioned mixed-mode test. For this, the machine stiffness, which may be imagined to be simulated by the spring controlling the displacement of the free end, is of the utmost importance. For example, if the machine stiffness is assumed to be infinite, the beam does not fail by a crack emanating from the notch tip but rather by a new crack that develops in the tension zone at the left support. However, if the machine has a finite stiffness, equivalent to a spring of stiffness $K = 3{,}000$ N/mm calibrated to fit both the numerical data and the correct crack propagation imagined at point B [see the inset figure in Fig. 6(b)], then a crack emanating from the notch tip is obtained in the simulations.

In this simulation, the same model free parameters and the finite-element size as in the Type 1 test are used. In Fig. 6(a), the experimentally observed crack pattern is superimposed on the finite-element mesh in which the crack appears in various shades. The darker the shade, the more open the crack is. Clearly, the
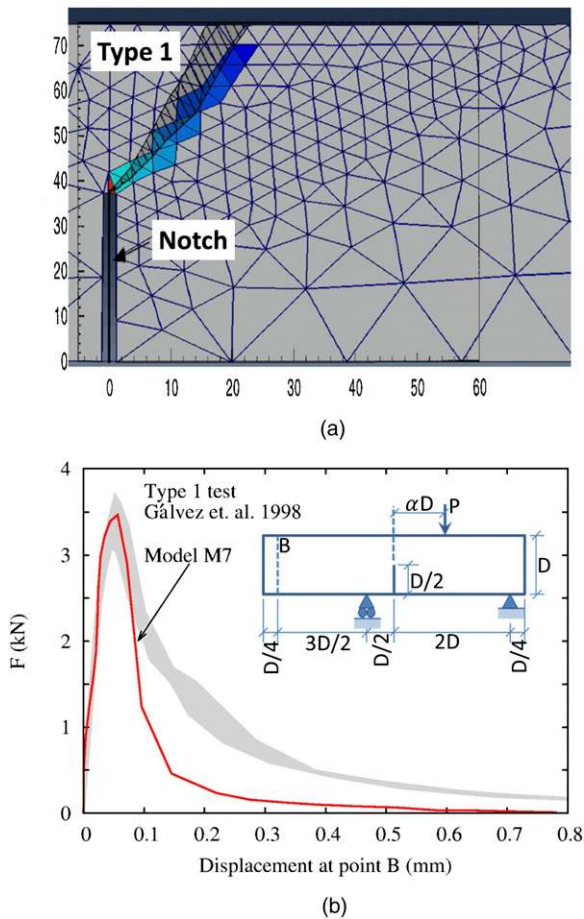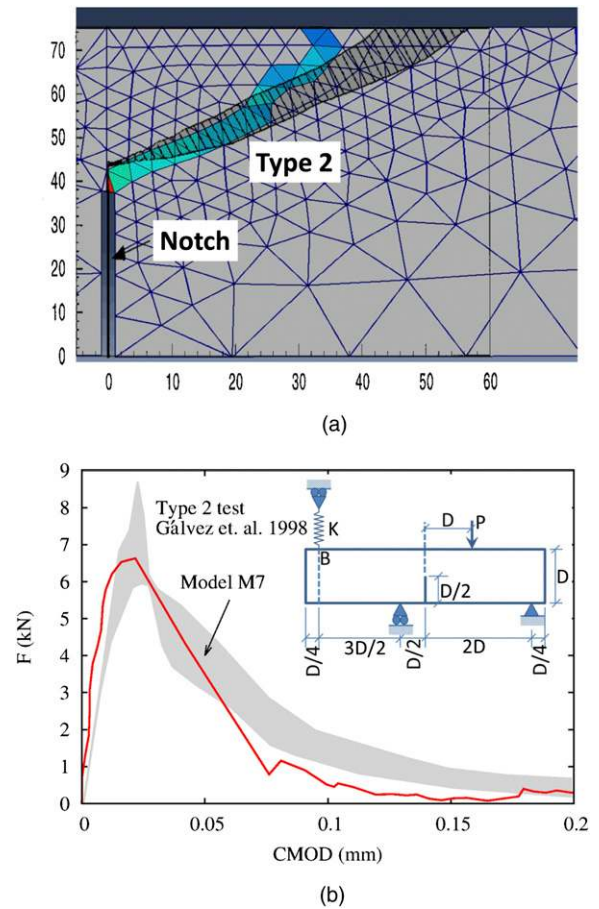
Fig. 5. Finite-element simulation of mixed-mode crack propagation and failure of asymmetrically notched three-point bend beam: (a) simulated and measured crack patterns; (b) simulated and measured load versus displacement at point B at the free end on the left of the beam [the test data and the inset figure of the test setup are from Gálvez et al. (1998)]


Fig. 6. Finite-element simulation of crack propagation and failure of asymmetrically notched three-point bend beam, with the displacement at a fourth point controlled to remain zero during the test: (a) simulated and measured crack patterns; (b) simulated and measured load versus crack mouth opening displacement (CMOD) [the test data and the inset figure of the test setup are from Gálvez et al. (1998)]

experimental and predicted cracks coincide. Fig. 6(b) compares the load versus the crack mouth opening displacement measured in the test to that predicted by model M7. The predicted response is in excellent agreement with the measured response.

The fourth problem analyzed is the mixed-mode crack propagation in the double-edge-notched specimen reported in Nooru-Mohamed (1992). The maximum aggregate size of the concrete used in the tests was 16 mm. This problem has been the subject of many studies. Many loading paths were used in experiments, and the path studied most frequently is chosen here. In this path, first the shear load of $F_h = 10$ kN is applied gradually while the vertical load is kept at $F_v = 0$. Second, a vertical tensile load F_v is raised up to failure while keeping the horizontal shear load constant at $F_h = 10$ kN.

This specimen is analyzed in 3D using random mesh with an average element size of 25 mm (which is roughly correct for strain localization according to the crack band model). The free model parameters used in the simulations are $E = 30,000$ MPa, $k_1 = 80 \cdot 10^{-6}$, $k_2 = 110$, $k_3 = 30$, $k_4 = 100$, and $k_5 = 1 \cdot 10^{-4}$. The finite-element size in this problem is chosen to be 16 mm. The crack paths experimentally observed on the front and back faces and the simulated crack paths are superimposed in Fig. 7(a). Their agreement is seen to be very good. Fig. 7(b) compares the measured data

to the curves of load versus gauge length displacement, as obtained by M7 and by other researchers (Gasser and Holzapfel 2006; Pivonka et al. 2004). The result by model M7 gives both the correct peak load and the correct crack paths. The reason for a less than perfect prediction of the load-displacement response must be small deviations from the observed crack path that have a large effect on the load-displacement response. For example, toward the end of the loading, the crack tip curves toward the direction of the tensile load instead of remaining perpendicular to it, which increases the load-carrying capacity relative to the test data. To avoid such problems, a finer mesh would be required, but that would require a nonlocal approach, which would in turn require knowing the material characteristic length. Determining this length would, however, necessitate data from corresponding size effect tests, which are lacking.

Finite-Element Check of Vertex Effect in M7

The fifth and last problem is a test in which the principal stress or strain axes rotate against the material. For such loading, which typically consists of axial compression followed by shear and is always produced by impacts, explosions, and earthquakes, the salient aspect is the vertex effect.
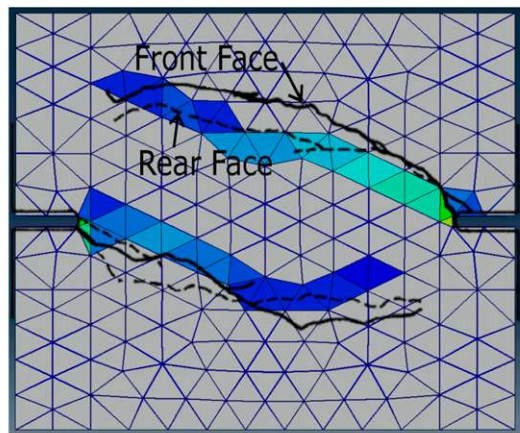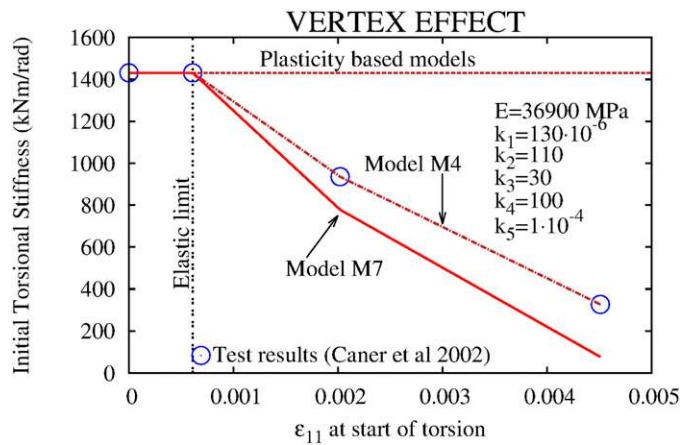
(a)
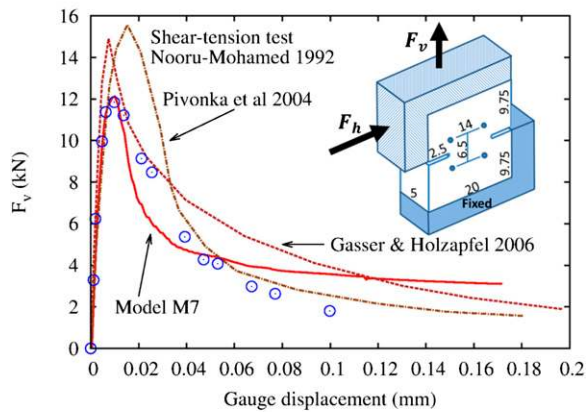
(b)

Fig. 7. Tension-shear test of double-edge-notched specimen of Nooru-Mohamed (1992) and its simulation by M7: (a) simulated and measured crack patterns; (b) simulated and measured vertical load versus gauge displacement [the test data are from Nooru-Mohamed (1992)]

(a)

(b)

Fig. 8. (a) Test data from vertex effect test with rotating principal axes and their simulation microplane models M4 and M7 and by plasticity-based models [the tests were performed by Caner et al. (2002)]; (b) vertex effect test specimen compressed first to an axial (postpeak) strain of 0.45% and next twisted about its axis at constant axial strain
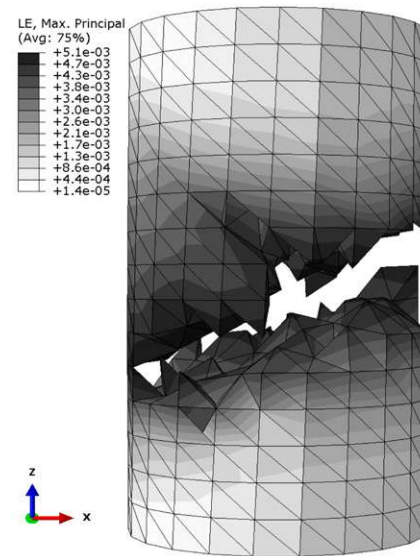
According to the tensorial incremental plastic or plastic-damage models, any load increment that is tangent to the current loading surface in the stress space should produce an elastic strain only. But it does not, and often, the tangential stiffness is several times smaller than the elastic stiffness (Bažant and Cedolin 1991; p. 500). The vertex effect, which was first discovered in metals (Gerard and Becker 1957; Budianski 1959), implies that, at the current state point in the stress space, either the loading surface must always have a corner (or vertex) traveling in the stress space with this point or that a multi-surface incremental plasticity in which multiple loading surfaces always intersect at the current state point to create a vertex. In either case, attempts to model the vertex effect tensorially were too complex and unsuccessful. In the computational practice after the 1980s, this effect has simply been ignored despite its practical importance.

Fortunately, the microplane models (as well as the Taylor models) exhibit this effect automatically (Brocca and Bažant 2000). This is not surprising, because the microplane models may be regarded as a variant of multisurface plasticity in which the loading surfaces (or stress-strain boundaries) are defined not in the tensorial space but vectorially on a generic plane.

In concrete, the vertex effect was experimentally discovered by Caner et al. (2002). Test cylinders of diameter 101.6 mm (4 in.) and length 203.2 mm (8 in.), with a maximum aggregate size of 9.5 mm, were used. The specimens were instrumented to measure axial and

torsional displacements using several LVDTs over a gauge length of 114.3 mm.

The loading path consisted of two parts. In the first part, some test cylinders were loaded under uniaxial compression up to the peak stress state, and others were loaded up to the postpeak states with axial strains 0.2 and 0.45%. In the second part of the load path, at one of these three strains, the cylinder was subjected to torsion while keeping the axial displacement constant, which created the vertex situation.

If the vertex effect did not exist, as implied by the current tensorial plastic and plastic-damage models, then the torsional stiffness would have to remain constant, corresponding to the horizontal line in Fig. 8(a). But the torsional stiffnesses measured by Caner et al. (2002), shown in this figure by the circled points, show a large decrease of torsional stiffness. For axial strain 0.45%, at which the uniaxial compressive stress is reduced to about 3/4 of the peak value, the elastic torsional stiffness, measured and reported in Caner et al. (2002), is reduced to a mere 1/4 of the elastic value. This is a major effect indeed.

The free model parameters used in this simulation are $E = 36,900$ MPa, $k_1 = 130 \cdot 10^{-6}$, $k_2 = 110$, $k_3 = 30$, $k_4 = 100$, and $k_5 = 1 \cdot 10^{-4}$. The finite-element size is chosen to be 15 mm. Fig. 8(b) shows the finite-element mesh used in the finite-element simulations and the maximum principal strain distribution in the cylinder for the case of a torsional (or vertex) loading that begins at the postpeak axial compressive strain of 0.45%. The results of M7 simulations, shown by the solid curve, give a somewhat stronger vertex effect than do the experiments, with somewhat greater reductions of the torsional stiffness. Simulations have also been made with the previous microplane model M4. That the M4 results match the data points exactly is probably by chance. The inevitable experimental error is probably as large as the deviation of the M7 curve from the data points. Also, using *ABAQUS*, generating a truly random mesh over the cylinder proved to be too difficult, and thus, the mesh bias must have affected the results in the simulations in which the model M7 was used.

Identification of Free Parameters and Scaling of Response

The meaning of each material parameter is briefly indicated in Tables 1 and 2. Changing the E-modulus to some other value E' causes a vertical scaling transformation (or affinity transformation) of all the response stress-strain curves such that all the stresses are multiplied by the ratio E'/E at no change of strains. (This is a vertical affinity transformation with respect to the strain axis.) Changing parameter k_1 to some other value k'_1 causes radial scaling of any stress-strain curve in which all the distances from the origin are multiplied by the ratio k'_1/k_1. (This is polar affinity transformation.)

If a vertical scaling by factor E'/E (obtained by replacing E by E') is combined with a radial scaling by factor $k_1 = E/E'$, the result is a horizontal scaling by factor k_1 of all the response curves. (This is a horizontal affinity transformation with respect to the stress axis.) These transformations do not change the shape of the response curves. The shapes are controlled by the remaining free parameters $k_2, \ldots, k_5$ and the fixed (hard-to-change) parameters $c_1, \ldots, c_{20}$.

The default values of the free parameters are listed in Table 2. Together with the values of fixed parameters listed in Table 1, they yield the uniaxial compression strength $f'_c = 36$ MPa (5,221.4 psi) and the axial normal strain at peak stress $\varepsilon_p = 0.0036$ as determined by simulation of the uniaxial compression test. If one needs a microplane model that yields the uniaxial compressive strength f^*_c and the corresponding strain at peak ε^*_p, it suffices to replace the reference values of parameters k_1 and E by the values

$$k^*_1 = k_1 \frac{\varepsilon^*_p}{\varepsilon_p}, \quad E^* = E \frac{f^*_c}{f'_c} \frac{\varepsilon_p}{\varepsilon^*_p} \quad (1)$$

Furthermore, the parameters listed in Tables 1 and 2 yield the following ratios characterizing the behavior of concrete:

$$f'_t/f'_c = 0.083, \quad f'_{bc}/f'_c = 1.4, \quad f^s_c/f'_c = 0.08 \quad (2)$$

where f'_c = uniaxial compressive strength; f'_t = uniaxial tensile strength; f'_{bc} = biaxial compressive strength; f^s_c = pure shear strength; $\sigma_r = 0$ = residual stress for very large uniaxial compressive strain; and $\tau_r = 0$ = residual stress for very large shear strain (at $\sigma_V = 0$). These ratios cannot be changed by the transformations according to Eq. (2). To change them, free parameters other than E and k_1 must be adjusted.

Striving to optimize the fits of extensive test data, one need not vary all five free parameters simultaneously. Starting with the given values of E and ν and assuming the reference values for all the other parameters, one can proceed in the following stages:

1. If sufficient data exist for the hydrostatic compression curve, fit this curve by adjusting only parameters k_3 and k_4. Otherwise, keep the default values.
2. Determine the radial scaling coefficient k_1 either simply from the strain at peak uniaxial compressive stress or better by fitting the complete uniaxial compressive stress-strain curve, postpeak included.
3. If sufficient data exist for triaxial compression with the confinement strong enough to make the response almost plastic (i.e., with no significant postpeak softening), fit them by adjusting k_2. Otherwise, keep the default value.
4. If sufficient data on uniaxial, biaxial, and triaxial compression exist for low hydrostatic pressures, fit them to obtain k_5. Otherwise, keep the default value.

Furthermore, by varying c_{17} (with k_1), one can control the tensile strength, and by varying $c_3, c_4, c_{13}, \ldots, c_{16}$, one can control the steepness of the postpeak slope in tension and in compression. Similarly, the postpeak slope in unconfined tension can be altered by changing c_3. Such optimizations, however, are not so easy, because other types of response also get affected.

Calibrating model M7 for a given concrete according to Steps 1–3 necessitates test data for only uniaxial compression, triaxial compression at various pressures, and hydrostatic compression. In many practical applications, except missile penetration and ground shock, the confining pressures are not high enough to cause pore collapse in concrete, which means that the compressive volumetric boundary does not matter. Then, Step 1 can be omitted, and parameters k_3 and k_4 have to be used at their default values, which means one needs to adjust only k_1 and k_2 according to Steps 2 and 3—an almost trivial task. Rarely, the user will have enough data to adjust k_5.

Are there too many parameters? Probably not if one takes note of the broad range of phenomena covered by the model. The von Mises material can do with only two parameters, but the metals it describes are incomparably simpler. Only one uniaxial stress-strain curve has to be matched. Here, one has about 20 different types of tests and must match dozens of curves. Mere fitting of these curves would require many dozens of parameters.

When only a few test types are considered in data fitting, the model has a high degree of ambiguity. This explains why a vast number of diverse nonlinear triaxial models for concrete are found in the literature. For an unambiguous result, all the present types of tests need to be considered in data fitting. In this regard, it may be noted that none of the important test data have been omitted from the current study even if their fits were not close.

Conclusions

1. The key idea of model M7 is to use the volumetric-deviatoric split of strain components only for the microplane stress-strain boundaries controlling the compressive behavior but not for the elastic stress and strain components and not for tensile boundary. This means that the volumetric and deviatoric boundaries are summed before being imposed on the total compressive normal stress.
2. This idea eliminates stress locking and excessive lateral strains in postpeak tensile softening and greatly improves the loading and unloading performance. It also allows modeling of the very high dilatancy observed in the frictional shear of low-strength concretes and the pronounced brittleness in high-strength concretes. It makes it possible to capture the

hardening response differences between high hydrostatic compression and compressive uniaxial strain. Importantly, it leads to a perfectly robust explicit algorithm for finite-element simulations. Compared with previous models, a much broader range of experimental data can be matched.

3. For data fitting, it is beneficial to deviate from the perfect kinematic constraint of the microplanes by making some microplane responses dependent on the volumetric part of the stress tensor and on the difference between the maximum and minimum principal strains. Although the former in theory breaks the explicitness of stress calculation, the algorithm remains explicit and performs well by taking the volumetric stress from the previous step.

4. The basic microplane formulation can be correlated with macrocontinuum potentials, which are distinct for the elastic regime, the tensile and compressive damage regimes, and the plastic-frictional regime. However, a rigorous thermodynamic formulation remains a challenge and deserves further debate.

5. The abandonment of the volumetric-deviatoric split of the elastic strains limits Poisson's ratio ν to values ≤ 0.25. This works for concrete. Materials with a higher ν can be easily simulated by coupling in parallel a simple fluidlike element with volumetric response only.

6. Because of the very broad range of behaviors simulated, there are many empirical material parameters. Five of them can easily be adjusted to fit the basic properties of a given concrete, and the remaining ones, which are hard to optimize, can be kept the same for all concretes.

7. Horizontal scaling of the inelastic postpeak part of the boundaries can be used as a way to implement the crack band model, to avoid spurious mesh sensitivity, and to ensure mesh-independent fracture energy in localized failure [Bažant and Caner 2005, Fig. 1 (left)].

8. The single material point fitting of stress-strain relations likely has no greater error than the optimum finite-element fitting, because no information exists on the material characteristic length or fracture energy of the concretes used and also because the information on the precise boundary conditions and precise gauge locations is missing or incomplete. Nevertheless, approximate delocalization with assumed characteristic length is applied to tensile softening data.

9. Model M7 can represent a considerably broader range of tests than other constitutive models for concrete, including: (1) the vertex effect, a feature of all microplane models (important especially for dynamics, where shear often suddenly follows postpeak compression); (2) the S-shaped unloading in tension, with transit into compression, and multiple hysteretic loops (important for earthquakes); (3) the difference in responses to extreme hydrostatic pressures and to extreme compression for rigidly confined uniaxial strain (important for missile impacts); (4) triaxial behavior under low, high, and very high confinement; and (5) biaxial behavior and uniaxial compressive behavior with correct loading and unloading cycles (which are very different from the tensile loading and unloading cycles).

Acknowledgments

References

ABAQUS 6.11 [Computer software]. Vélizy-Villacoublay, France, Dassault Systèmes.

Balmer, G. G. (1949). "Shearing strength of concrete under high triaxial stress computation of Mohr's envelope as a curve." *Rep. No. SP-23*, Structural Research Laboratory, Bureau of Reclamation, U.S. Dept. of the Interior, Denver.

Bažant, Z., and Yu, Q. (2011). "Size effect testing of cohesive fracture parameters and non-uniqueness of work-of-fracture method." *J. Eng. Mech.*, 137(8), 580–588.

Bažant, Z. P., Bishop, F. C., and Chang, T.-P. (1986). "Confined compression tests of cement paste and concrete up to 300 ksi." *J. Am. Concr. Inst.*, 33(4), 553–560.

Bažant, Z. P., and Caner, F. C. (2005). "Microplane model M5 with kinematic and static constraints for concrete fracture and anelasticity. II. Computation." *J. Eng. Mech.*, 131(1), 41–47.

Bažant, Z. P., and Cedolin, L. (1991). *Stability of structures: Elastic, damage theories*, Oxford University Press, New York.

Bažant, Z. P., and Oh, B.-H. (1983). "Crack band theory for fracture of concrete." *Matér. Struct.*, 16(3), 155–177.

Bažant, Z. P., and Oh, B.-H. (1986). "Efficient numerical integration on the surface of a sphere." *Z. Angew. Math. Mech.*, 66(1), 37–49.

Bažant, Z. P., Xiang, Y., Adley, M. D., Prat, P. C., and Akers, S. A. (1996). "Microplane model for concrete. II. Data delocalization and verification." *J. Eng. Mech.*, 122(3), 255–262.

Bresler, B., and Pister, K. S. (1958). "Strength of concrete under combined stresses." *J. Am. Concr. Inst.*, 551(9), 321–345.

Brocca, M., and Bažant, Z. P. (2000). "Microplane constitutive model and metal plasticity." *Appl. Mech. Rev.*, 53(10), 265–281.

Budianski, B. (1959). "A reassessment of deformation theories of plasticity." *J. Appl. Mech.*, 26(2), 259–264.

Caner, F., Bažant, Z., and Červenka, J. (2002). "Vertex effect in strain-softening concrete at rotating principal axes." *J. Eng. Mech.*, 128(1), 24–33.

Caner, F. C., and Bažant, Z. P. (2013). "Microplane model M7 for plain concrete. I: Formulation." *J. Eng. Mech.*, 139(12), 1714–1723.

Chern, J.-C., Yang, H.-J., and Chen, H.-W. (1992). "Behavior of steel fiber-reinforced concrete in multiaxial loading." *ACI Mater. J.*, 89(1), 32–40.

Cusatis, G., Bažant, Z. P., and Cedolin, L. (2003). "Confinement–shear lattice model for concrete damage in tension and compression: I. Theory." *J. Eng. Mech.*, 129(12), 1439–1448.

Cusatis, G., Mencarelli, A., Pelessone, D., and Baylot, J. T. (2011a). "Lattice discrete particle model (LDPM) for failure behavior of concrete. II: Calibration and validation." *Cement Concr. Compos.*, 33(9), 891–905.

Cusatis, G., Pelessone, D., and Mencarelli, A. (2011b). "Lattice discrete particle model (LDPM) for failure behavior of concrete. I: Theory." *Cement Concr. Compos.*, 33(9), 881–890.

Gálvez, J., Elices, M., Guinea, G., and Planas, J. (1998). "Mixed mode fracture of concrete under proportional and nonproportional loading." *Int. J. Fract.*, 94(3), 267–284.

Gasser, T. C., and Holzapfel, G. A. (2006). "3D crack propagation in unreinforced concrete: A two-step algorithm for tracking 3D crack paths." *Comput. Methods Appl. Mech. Eng.*, 195(37–40), 5198–5219.

Gerard, G., and Becker, H. (1957). "Handbook of structural stability: Part I. Buckling of flat plates." *NACA Technical Note 3781*, National Advisory Committee for Aeronautics, Washington, DC.

Green, S. J., and Swanson, S. R. (1973). "Static constitutive relations for concrete." *Rep. No. AFWL-TR-72-2*, Air Force Weapons Laboratory, Kirtland Air Force Base, Albuquerque, NM.

Jirásek, M., and Zimmermann, T. (1998). "Analysis of rotating crack model." *J. Eng. Mech.*, 124(8), 842–851.

Kupfer, H., Hilsdorf, H. K., and Rüsch, H. (1969). "Behavior of concrete under biaxial stresses." *J. Am. Concr. Inst.*, 66(8), 656–666.

Launay, P., and Gachon, H. (1971). "Strain and ultimate strength of concrete under triaxial stress." *Proc., 1st Int. Conf. on Structural Mechanics in Reactor Technology (SMiRT1)*, T. Jaeger, ed., Commission of European Communities, Brussels, Belgium.

Li, F., and Li, Z. (2000). "Continuum damage mechanics based modeling of fiber-reinforced concrete in tension." *Int. J. Solids Struct.*, 38(5), 777–793.

Li, Z., Li, F., Chang, T.-Y.-P., and Mai, Y.-W. (1998). "Uniaxial tensile behavior of concrete reinforced with randomly distributed short fibers." *ACI Mater. J.*, 95(5), 564–574.

Nooru-Mohamed, M. (1992). "Mixed mode fracture of concrete: An experimental approach." Ph.D. thesis, Delft Univ. of Technology, Delft, Netherlands.

Petersson, P. E. (1981). "Crack growth and development of fracture zones in plain concrete and similar materials." *Rep. No. TVBM 1006*, Lund Institute of Technology, Lund, Sweden.

Pivonka, P., Ožbolt, J., Lackner, R., and Mang, H. A. (2004). "Comparative studies of 3D-constitutive models for concrete: Application to mixed-mode fracture." *Int. J. Numer. Methods Eng.*, 60(2), 549–570.

Reinhardt, H. W., and Cornelissen, H. A. W. (1984). "Post-peak cyclic behavior of concrete in uniaxial tensile and alternating tensile and compressive loading." *Cement Concr. Res.*, 14(2), 263–270.

Sinha, B. P., Gerstle, K. H., and Tulin, L. G. (1964). "Stress-strain relations for concrete under cyclic loading." *J. Am. Concr. Inst.*, 62(2), 195–210.

van Mier, J. G. M. (1984). "Strain-softening of concrete under multi-axial loading conditions." Ph.D. thesis, Die Technische Hogeschool Eindhoven, Eindhoven, Netherlands.

van Mier, J. G. M. (1986a). "Multiaxial strain-softening of concrete. I: Fracture." *Mater. Struct.*, 19(3), 179–190.

van Mier, J. G. M. (1986b). "Multiaxial strain-softening of concrete. II: Load histories." *Mater. Struct.*, 19(3), 190–200.

Yin, W. S., Su, E. C. M., Mansur, M. A., and Hsu, T. T. C. (1989). "Biaxial tests of plain and fiber concrete." *ACI Mater. J.*, 86(3), 236–243.